Available online at www.CivileJournal.org

Civil Engineering Journal

(E-ISSN: 2476-3055; ISSN: 2676-6957)

Vol. 12, No. 02, February, 2026

From Corrosion to Collapse: Spatiotemporal Evolution of Local Stability in Anchored Anti-Dip Slopes

Ding-Jian Wang [1, 2], Qian-Yun Wang [1, 2], Zhi-Qiang Fan [3], Fang Ouyang [1*], Ya-Hui Zhang [2]

[1] *Institute of Engineering Disaster Prevention and Mitigation, Hubei University of Education, Wuhan 430205, China.*

[2] *Faculty of Engineering, China University of Geosciences, Wuhan 430074, China.*

[3] *PowerChina Huadong Engineering Corporation Limited, Hangzhou 310014, China.*

Received 18 November 2025; Revised 19 January 2026; Accepted 23 January 2026; Published 01 February 2026

Abstract

The long-term stability of anchored anti-dip slopes in hydropower and mining projects is threatened by corrosion-induced degradation of rock bolt systems. Existing deterministic models relying on global safety factors fail to capture localized failure mechanisms and inherent geotechnical uncertainties. This study aims to develop a probabilistic framework for assessing the spatiotemporal stability evolution of such slopes under progressive bolt corrosion. A novel Factor of Local Safety (FoLS) is introduced to quantify stability at individual rock column levels, enabling spatially explicit assessment. This metric is integrated with a time-variant mechanical model for bolt capacity loss and Monte Carlo simulation for uncertainty propagation. Applied to a representative slope, the framework reveals complex degradation patterns: failure initiates in the extremely active toppling zone, progresses to the moderately active zone, and ultimately extends to the passive and shear sliding zones. Sensitivity analyses highlight the critical influence of bolt inclination, yield strength, bolt-rock bond strength, and grout water-cement ratio. Comparative anchorage scenarios demonstrate the superior long-term effectiveness of lower-bench reinforcement. The study provides a novel, spatially differentiated approach for the design, maintenance, and risk management of anchored anti-dip slopes, emphasizing the necessity of dynamic stability monitoring over time.

Keywords: Anti-Dip Slope; Rock Bolt Corrosion; Spatiotemporal Stability; Probabilistic Assessment; Factor of Local Safety.

1. Introduction

Anchored anti-dip rock slopes are fundamental to the safe operation of major hydroelectric and mining projects worldwide [1-3]. Characterized by rock strata dipping into the hillside, these slopes are inherently susceptible to flexural toppling failure, a progressive deformation mechanism that poses a persistent threat to infrastructure with design lifespans often exceeding a century [4, 5]. Rock bolting serves as the primary engineering intervention, designed to transfer driving forces from potentially unstable surficial rock to competent bedrock beneath a deep-seated failure surface [6-8]. Representative cases of such engineered slopes are illustrated in Figure 1. However, the perennial challenge to this paradigm is the inevitable environmental degradation of the steel anchoring elements. Field exhumations and inspections have consistently documented significant corrosion in rock bolts and cables after decades of service, particularly in environments subject to water-level fluctuations and groundwater seepage [9, 10]. This corrosion-induced deterioration of the support system precipitates a gradual yet consequential decay in

* Corresponding author: foy1694@hue.edu.cn

https://doi.org/10.28991/CEJ-2026-012-02-01

slope stability, transforming a static design problem into a dynamic, time-variant risk [11-15]. Consequently, transitioning from a conventional deterministic assessment to a spatiotemporal probabilistic framework is imperative for predicting the pathway from corrosion to collapse and ensuring the long-term resilience of these critical geotechnical structures.

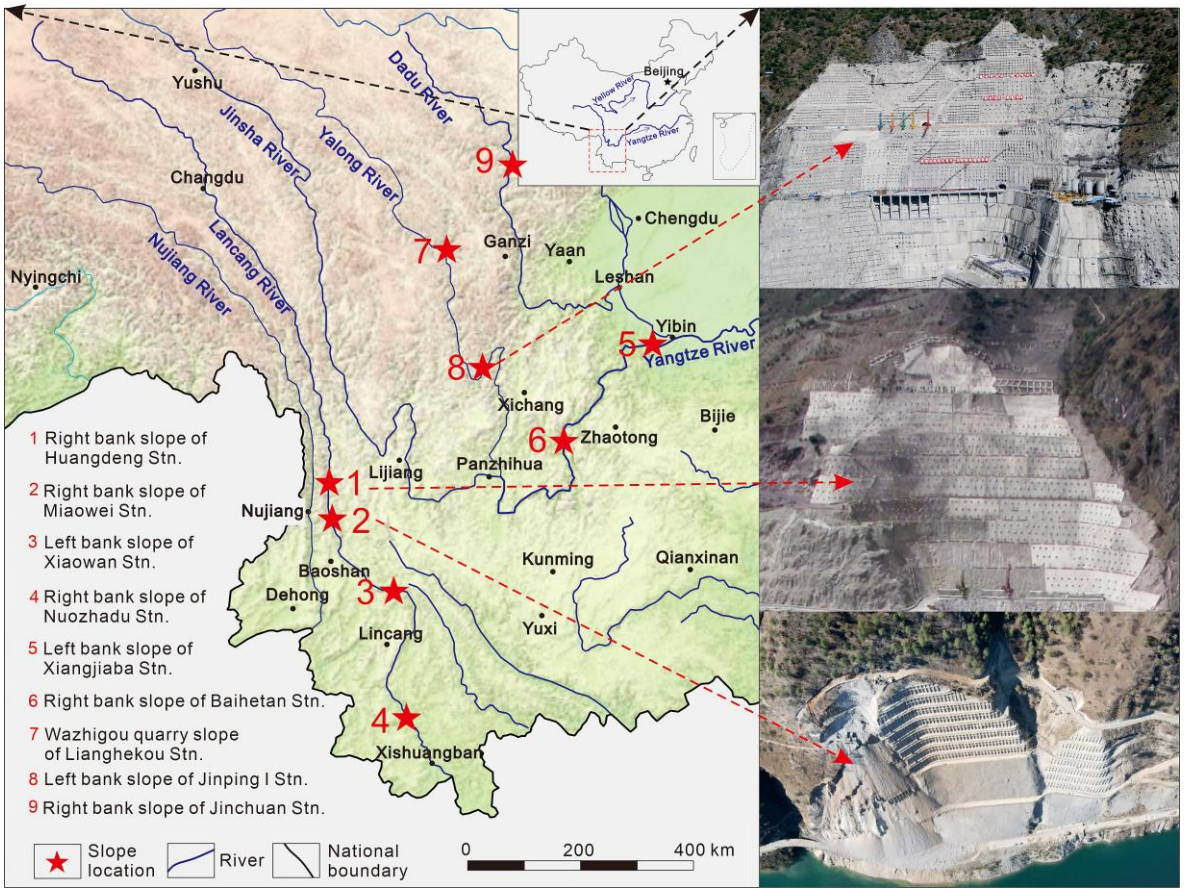

Figure 1. Representative anchored anti-dip rock slopes in hydropower projects, Southwest China

Extensive research, based on field geological surveys and physical model tests, has summarized the deformation and failure mechanisms of anti-dip slopes [16-19]. Subsequent theoretical and numerical studies have focused primarily on three areas: (1) mechanical analysis models for various failure modes, including block toppling, flexural toppling and flexural-block toppling [20-23]; (2) failure processes under specific conditions such as earthquake and excavation [18, 24, 25]; and (3) long-term evolutionary behaviors [26-28].

Although anti-dip slopes are generally regarded as more stable than pro-dip slopes, research on their anchorage remains comparatively limited. Recent studies have mainly addressed anchor force calculations, optimization of bolt layouts for stability enhancement, and failure processes during excavation or seismic events. Notable contributions include: analytical models for anchored block toppling slopes [29] and anchored flexural toppling slopes [30]; determination of optimal bolt inclination in toppling rock masses based on laboratory experiments [31]; physical model tests [32] and discontinuous deformation analysis (DDA) [33] of failure mechanisms in slopes reinforced with Negative Poisson's Ratio (NPR) bolts; discrete element analysis of cable stress states and slope deformation under varying anchor arrangements [34]; and shaking table tests revealing seismic failure mechanisms [35]. These studies provide profound insights into the failure mechanisms of anchored anti-dip slopes. Critically, however, they have neglected the corrosion process of bolts/cables, leaving models for long-term stability evolution unestablished.

Despite these advancements, existing stability assessments for anchored anti-dip slopes are predominantly characterized by three limitations: (1) Evaluations depend overwhelmingly on a global Factor of Safety (FoS), which obscures the spatial heterogeneity of stability and fails to identify localized precursor zones of failure. (2) Most models are deterministic, neglecting the intrinsic variability of geological and material parameters, thereby offering no probabilistic measure of risk evolution over a slope's operational lifetime. (3) The corrosion process of the bolts themselves is routinely decoupled from the mechanical slope model. Studies that incorporate corrosion often apply simplified, empirical models without integrating them into a spatially explicit mechanical framework for local stability evolution. A comprehensive methodology that quantifies how localized corrosion propagates into spatially differentiated stability loss and, ultimately, global failure remains conspicuously absent.

To bridge these identified gaps, this study develops an integrated probabilistic framework for decoding the spatiotemporal evolution of local stability in anchored anti-dip slopes under bolt corrosion. A novel metric - Factor of Local Safety (FoLS) - is introduced to quantify stability at the scale of individual rock columns, enabling spatially granular assessment. A coupled time-dependent mechanical model is established, integrating a limit-equilibrium analysis of flexural toppling with the progressive degradation of bolt tensile capacity, the latter governed by empirical corrosion kinetics. A Monte Carlo simulation-based probabilistic framework is implemented to propagate input uncertainties, yielding full distributions of FoLS and local failure probability across the slope profile and over time. Applied to a detailed case study, the framework elucidates the corrosion-driven failure mechanism, quantifies spatiotemporal degradation patterns, and offers practical insights for the design, monitoring, and risk-informed management of anchored anti-dip slopes.

2. Corrosion-Induced Failure of Rock-Bolt System

2.1. Corrosion Process of Rock Bolts

Flexural toppling failure in anti-dip slopes typically involves a deep-seated potential failure surface within the rock masses. From this failure surface towards the slope face, the bending deformation of the rock strata progressively intensifies, inducing interlayer dislocation. The stabilizing process for anti-dip slopes commonly involves excavating and removing the shallow, fractured rock mass down to fresh bedrock. Rock bolts/cables are subsequently installed deep into the slope, with their bonded lengths securely anchored in the stable bedrock beneath the potential failure surface (Figure 2). The slope face is typically excavated into a stepped configuration and sprayed with shotcrete to prevent surface erosion.

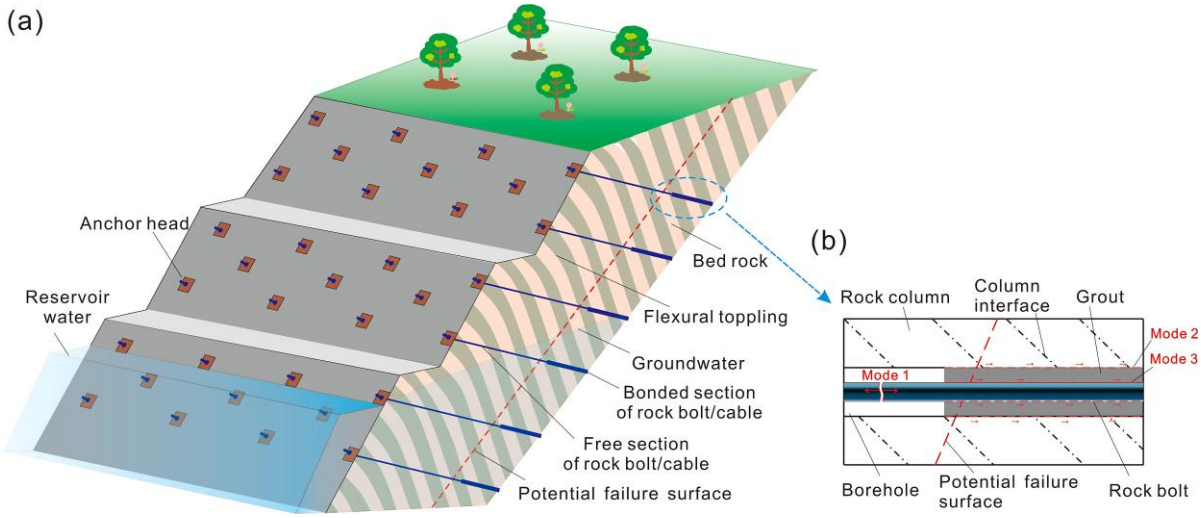

Figure 2. (a) Schematic of an anchored anti-dip; (b) Failure modes of the rock-bolt system

Exposure to environmental factors such as reservoir water fluctuations, rainfall infiltration, and groundwater leads to corrosion on various components of the anchorage structure. Field investigations involving the excavation of anchors after years of service [9, 10] have confirmed the occurrence of this corrosion. Morphological observations indicate that corrosion at the anchor head and within the free length of the bolt is generally more severe than within the bonded length (Figure 3).

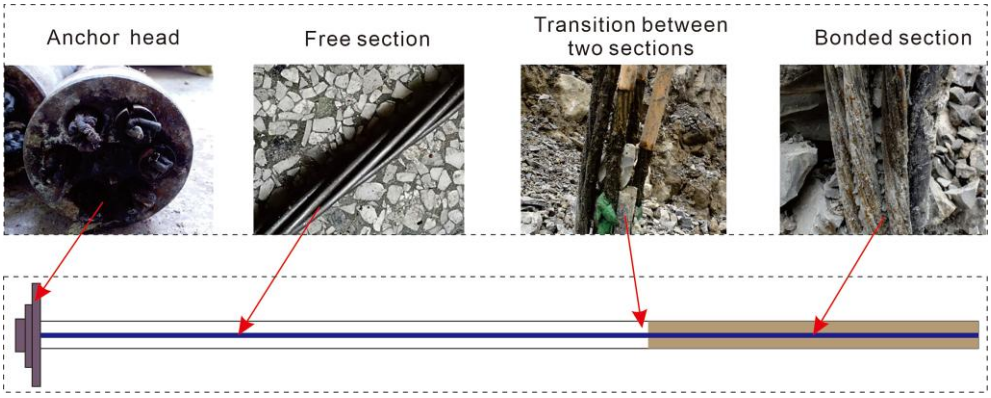

Figure 3. Morphology of anchor corrosion at the Shaping-II excavation site (after [9])

Failure of the rock-bolt system manifests primarily in four modes [36]: tensile yield failure of the rock bolt, shear failure at the bolt-grout interface, shear failure at the grout-rock interface, and failure of the surrounding rock mass. These failure modes have been validated or recognized in numerous subsequent studies [37, 38]. In anti-dip rock slopes, the strength of the intact rock typically far exceeds the bond strength at the interfaces between the bolt, grout, and rock. Consequently, this study focuses primarily on the first three failure modes (Figure 2-b). Furthermore, when analyzing the impact of environmental corrosion on the slope-anchorage system, the emphasis is placed on the corrosion process of the bolts themselves, disregarding potential deterioration of the rock masses or grout materials.

Although numerous experimental studies exist on rock bolt corrosion, a theoretical model capable of accurately predicting bolt corrosion rates remains elusive. Some studies [39-41] have adopted a modified corrosion rate model for steel reinforcement in concrete structures, originally proposed by Vu & Stewart [42], to describe the corrosion-induced degradation process of rock bolts. This model accounts for the influence of grout cover thickness and the water-cement ratio of the grout, assumed to be the primary factors governing the corrosion rate. Assuming uniform corrosion under typical environmental conditions (75% relative humidity, 20°C), the radial corrosion rate of the bolt (i_{corr}, in m/year) is expressed as:

$$i_{\text{corr}}(t) = 3.727 \times 10^{-7} \frac{(1-r_{\text{wc}})^{-1.64} t^{-0.29}}{d_c} \tag{1}$$

where, d_c is the grout cover thickness, r_{wc} is the mass ratio of water to cement in the grout, and t is the exposure time with the unit in years. Unless otherwise specified, all parameters in this paper utilize fundamental SI units.

The radial corrosion depth of the bolt (Δd) over time period t can be obtained by integration:

$$\Delta d(t) = \int_0^t i_{\text{corr}}(t)dt = 5.249 \times 10^{-7} \frac{(1-r_{\text{wc}})^{-1.64}}{d_c} t^{0.71} \tag{2}$$

It is acknowledged that the Vu-Stewart model was originally developed for steel reinforcement in concrete. Its transfer to grouted rock bolts involves environmental differences, such as potentially distinct oxygen availability, moisture transport mechanisms, and cracking patterns in the grout column compared to concrete. While these factors may influence the absolute corrosion rate, the model's functional form, which links rate to grout cover and water-cement ratio, captures the primary protective effect of the grout. Its adoption in this study follows precedent in rock slope anchorage literature [39, 43], where it has been used as a validated engineering approximation for long-term degradation assessment when site-specific data is limited.

2.2. Tensile Capacity Prediction of Rock-Bolt System Undergoing Corrosion

The tensile forces corresponding to the three failure modes must first be calculated. The tensile capacity of the rock-bolt system is then determined by comparing these forces. Considering corrosion effects, the tensile capacity of the bolt under each failure mode throughout its service life is presented below.

(i) Tensile yield failure of rock bolt

Bolts subjected to prolonged exposure in humid environments experience radial corrosion progressing inward from the outer surface. This corrosion reduces the bolt's effective cross-sectional area and concurrently degrades the yield strength of the steel material. Tensile yield failure occurs when the tensile stress in the bolt exceeds its residual yield strength. The time-dependent ultimate tensile capacity of the corroding bolt (T_a) is given by [39, 40]:

$$T_a(t) = \frac{\pi}{4} d_0^2 [1 - \eta_s(t)] f_s \alpha_s(t) \tag{3}$$

where d_0 is the initial bolt diameter, f_s is the initial yield strength of the bolt steel, η_s is the loss rate of the bolt's cross-sectional area due to corrosion, and α_s is the strength reduction coefficient of the bolt steel, defined as the ratio of the yield strength at time t to the initial yield strength. The expressions for η_s and α_s are as follows [44]:

$$\eta_s(t) = \frac{{d_0}^2 - [d_0 - 2\Delta d(t)]^2}{{d_0}^2} \tag{4}$$

and

$$\alpha_s(t) = \begin{cases} 1 & \text{for } \eta_s(t) \le 5\% \\ \frac{0.985 - 1.028\eta_s(t)}{1-\eta_s(t)} & \text{for } \eta_s(t) > 5\% \end{cases} \tag{5}$$

Equations 4 and 5 indicate that when the cross-sectional area loss rate is below 5%, the tensile capacity reduction is governed primarily by the area loss. However, when the loss rate exceeds 5%, the tensile capacity is significantly influenced by both the area loss and the inherent degradation of the steel's yield strength.

(ii) Shear failure at bolt-grout interface

Under axial tension, the force in the bolt is transferred to the grout as shear stress through the bond at the bolt-grout interface. Bolt corrosion degrades the shear strength of this interface bond. If the bond's shear capacity drops below the tensile force in the bolt, shear failure occurs at the bolt-grout interface. According to the strength criterion, the ultimate tensile force (T_b) that the bolt-grout bond can sustain without failure is:

$$T_b(t) = \pi d_0 L_{\mathrm{bg}} \tau_{\mathrm{bg}} r_{\mathrm{bg}}(t) \tag{6}$$

where, L_{bg} is the effective bond length between the bolt and the grout, τ_{bg} is the initial shear strength of the bolt-grout bond, and r_{bg} is the reduction coefficient of the bolt-grout bond strength, defined as the ratio of the bond strength at time t to the initial bond strength.

Numerous experimental and theoretical studies have investigated the degradation of steel-concrete bond strength under corrosion [45, 46]. Existing literature primarily utilizes two indicators for real-time bond strength assessment: steel mass loss and concrete surface crack width. This study adopts the empirical model proposed by Bhargava et al. [47] for bond strength prediction, which was derived from fitting extensive steel pull-out test results and has been applied to rock bolt corrosion studies. Assuming the density of the uncorroded core remains unchanged, the reduction coefficient r_{bg} satisfies:

$$r_{\mathrm{bg}}(t) = \begin{cases} 1 & \text{for } \eta_s(t) \le 1.5\% \\ 1.192 \times e^{-11.7\,\eta_s(t)} & \text{for } \eta_s(t) > 1.5\% \end{cases} \tag{7}$$

Equation 7 shows that the bolt-grout bond strength remains constant when the bolt's cross-sectional area loss is less than 1.5%. However, once the loss rate exceeds 1.5%, the bond strength decreases exponentially. The applicability of the Bhargava model for rock bolt systems has been confirmed in relevant studies [48-50].

(iii) Shear failure at rock-grout interface

The tensile force in the bolt is ultimately transferred to the bedrock of the slope through shear action at the grout-rock interface. If this force exceeds the bond strength at the grout-rock interface, the rock-bolt system fails in shear along this interface. According to the strength criterion, the ultimate tensile force (T_c) that the grout-rock bond interface can sustain is [41]:

$$T_c = \pi D_0 L_{\mathrm{gr}} \tau_{\mathrm{gr}} \tag{8}$$

where, D_0 is the borehole diameter (representing the interface diameter), L_{gr} is the effective bond length of the grout-rock interface, and τ_{gr} is the corresponding interface shear strength. As stated in Section 2.1, this study considers only bolt corrosion, neglecting deterioration of the rock or grout. Therefore, T_c is assumed constant relative to time.

The analysis above establishes the time-dependent ultimate tensile capacities of the rock-bolt system under the three primary failure modes. Under actual working conditions, the system's overall tensile capacity follows the "weakest-link" principle. That is, the tensile capacity (T) of the integrated rock-bolt system is governed by the minimum value among the capacities under the three failure modes. System failure occurs once the actual tensile force exceeds T:

$$T(t) = min\{T_a,\ T_b,\ T_c\} \tag{9}$$

Substituting Equations 1 to 8 into Equation 9 reveals that T depends primarily on three categories of parameters, those are material parameters (f_s, τ_{bg}, τ_{gr}, r_{wc}), geometric parameters (d_0, D_0, d_c, L_{bg}, L_{gr}), and the duration of corrosion exposure (t). This model for calculating the bolt system's tensile capacity under corrosion will be utilized for the subsequent evaluation of slope flexural toppling stability.

3. Local Stability Analysis of Anchored Anti-Dip Slope

Toppling failure in anti-dip slopes manifests primarily in three distinct modes: flexural toppling, block toppling, and flexural-block toppling [20-23]. Anchored anti-dip slopes in large-scale hydropower projects are predominantly susceptible to flexural toppling. Notably, even when encountering naturally occurring blocky slopes, unstable shallow blocks are typically excavated and removed prior to anchorage installation. Consequently, the mechanical model developed herein specifically addresses the stability of anchored slopes undergoing flexural toppling.

Conventional stability evaluations for flexural toppling slopes, whether deterministic or probabilistic, predominantly rely on the concept of global stability, quantified by the Factor of Safety (FoS), with scant attention to localized stability assessment [51]. To address this gap, this study establishes a novel mechanical analysis framework specifically designed for evaluating the local stability of anchored flexural toppling slopes. This framework facilitates the effective identification of stability states at discrete locations along the slope profile, enabling targeted reinforcement strategies.

3.1. Mechanical Analysis

Results from laboratory model tests and numerical simulations [32-35] indicate that while anchored anti-dip slopes exhibit significantly enhanced stability compared to their unanchored counterparts, their fundamental failure modes remain analogous with differences in fracturing confined to localized regions. A critical feature of flexural toppling slopes is the existence of a deep-seated potential failure surface, whose dip angle is slightly greater than the inclination of the normal to the rock columns. The rock masses above this potential surface are subdivided into three distinct zones from slope toe to crest: the shear sliding zone, the flexural toppling zone, and the stable zone (Figure 4-a) [30]. Crucially, the potential failure surface differs from the actual fracture surfaces of the individual rock columns. The actual fracture surface of a column is oriented perpendicular to its edges, collectively forming a stepped failure profile, whereas the potential failure surface represents a conceptual plane connecting the midpoints of these actual fracture surfaces (Figure 4-b). The bonded length of each rock bolt is securely anchored within the stable bedrock beneath the potential failure surface, while the bolt head is fixed on the slope face. This configuration enables the transfer of driving forces from the upper rock mass to the stable bedrock via the restraining action between the bolt head and the bonded length [32, 35].

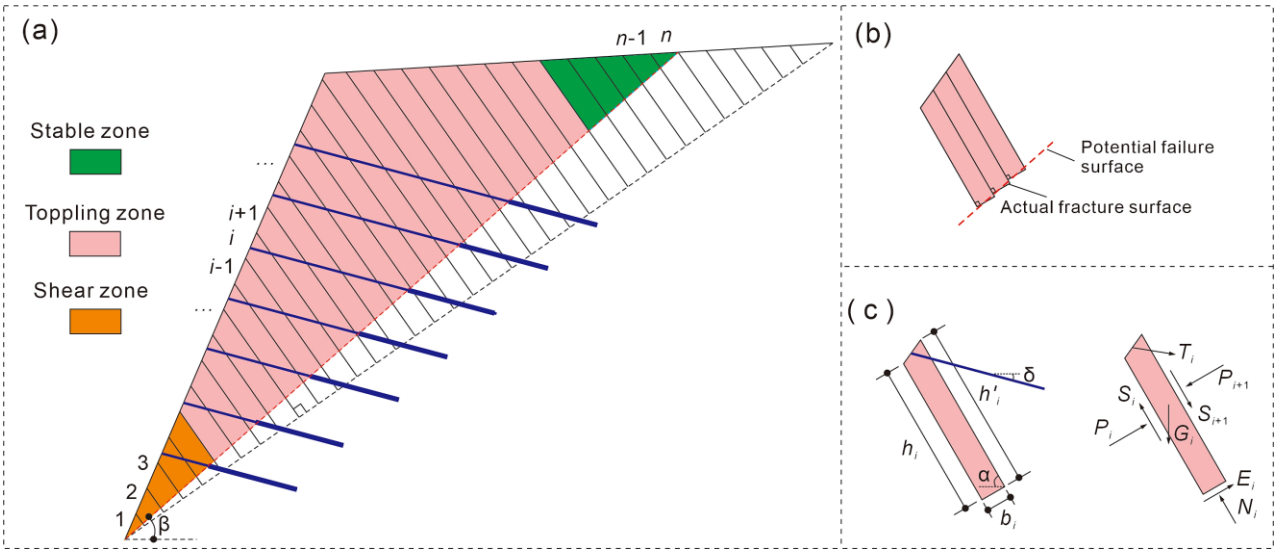

Figure 4. (a) Schematic profile of an anchored anti-dip slope depicting deformation zones; (b) Relationship between the potential failure surface and actual fracture surfaces of rock columns; (c) Geometry and force system acting on a representative rock column *i*.

Rock columns are sequentially numbered from 1 at the slope toe to *n* at the slope crest. Consider the force equilibrium of the *i*-th column, as illustrated in Figure 4-c. The acting forces comprise: gravitational force (G_i), thrust forces from adjacent upper and lower columns (P_{i+1}, P_i), frictional shear forces along column interfaces (S_{i+1}, S_i), normal and shear reactions from the underlying bedrock (N_i, E_i), and the tensile force in the installed rock bolt (T_i). T_i is equal to zero if no bolt is present at the top of column *i*.

(i) For column *i* in the shear sliding zone

Force equilibrium must be satisfied in directions parallel and perpendicular to the column interfaces:

$$G_i \sin\alpha + T_i \cos(\alpha - \delta)/w_i - N_i - S_i + S_{i+1} = 0 \quad (10)$$

$$P_{i+1} - P_i + G_i \cos\alpha - T_i \sin(\alpha - \delta)/w_i - R_i = 0 \quad (11)$$

where, α is the angle of the column interface to the horizontal, δ is the inclination of the bolt, and w is the horizontal bolt spacing. R and S satisfy the Coulomb criterion: $R_i = N_i \tan\varphi_i$ and $S_i = P_i \tan\varphi'_i$, where φ_i and φ'_i are the friction angles of the rock base and the column interface, respectively. Combining Equations 10 and 11 yields the inter-column thrust relationship:

$$\lambda_i^s P_{i+1} - \kappa_i^s P_i + \varepsilon_i^s G_i - \mu_i^s T_i = 0 \quad (12)$$

The coefficients λ_i^s, κ_i^s, ε_i^s and μ_i^s are defined as:

$$\lambda_i^s = 1 - \tan\varphi'_{i+1} \tan\varphi_i \quad (13)$$

$$\kappa_i^s = 1 - \tan\varphi'_i \tan\varphi_i \quad (14)$$

$$\varepsilon_i^s = cos\,\alpha - sin\,\alpha\,tan\,\varphi_i \quad (15)$$

$$\mu_i^s = [sin(\alpha - \delta) + cos(\alpha - \delta)\,tan\,\varphi_i]/w_i \quad (16)$$

(ii) For column *i* in the flexural toppling or stable zone:

A cantilever beam model is typically employed, assuming the column remains intact prior to failure. Failure occurs when the induced bending moment exceeds the column's flexural capacity, governed by the tensile strength criterion:

$$\frac{M_i b_i}{2I_i} - \frac{N_i}{b_i} = \sigma_i^t \quad (17)$$

where, M is the net bending moment acting on the column base, N is the net axial force (positive in compression), b is the column width, I is the moment of inertia of the column cross-section ($I_i = b_i^3/12$ for a square column in 2-dimension), and σ^t is the tensile strength of the rock. Based on the force analysis in Figure 4-c, the bending moment M_i at the base is:

$$M_i = \frac{1}{2}G_i\bar{h}_i\,cos\,\alpha + \eta P_{i+1}h'_i - \eta P_i h_i - \frac{1}{2}P_{i+1}b_i\,tan\,\varphi'_{i+1} - \frac{1}{2}P_i b_i\,tan\,\varphi'_i - T_i\bar{h}_i sin(\alpha - \delta) \quad (18)$$

Substituting Equation 17 and simplifying leads to:

$$\lambda_i^t P_{i+1} - \kappa_i^t P_i + \varepsilon_i^t G_i - \mu_i^t T_i - b_i^2\sigma_i^t = 0 \quad (19)$$

The coefficients λ_i^t, κ_i^t, ε_i^t and μ_i^t are defined as:

$$\lambda_i^t = 6\eta h'_i - 4b_i\,tan\,\varphi'_{i+1} \quad (20)$$

$$\kappa_i^t = 6\eta h_i + 2b_i\,tan\,\varphi'_i \quad (21)$$

$$\varepsilon_i^t = 3\bar{h}_i\,cos\,\alpha - b_i\,sin\,\alpha \quad (22)$$

$$\mu_i^t = \left[6\bar{h}_i\,sin(\alpha - \delta) + b_i\,cos(\alpha - \delta)\right]/w_i \quad (23)$$

Equations 12 and 19 establish the fundamental relationships between the thrust forces (P_{i+1}, P_i) on the boundaries of a single rock column. While G_i is directly calculable and T_i is derived from the model in Section 2, stability analysis requires iterative computations of thrust forces across all columns. Critically, the boundaries between the shear sliding zone, flexural toppling zone, and stable zone must be identified prior to initiating the thrust force iteration.

3.2. Identification of Zone Boundaries

The boundary between the flexural toppling zone and the stable zone can be readily determined. Utilizing Equation 19, iterate downwards starting from the topmost column (n). The interface between column j and j+1 where the calculated thrust $P_j > 0$ first occurs defines this boundary.

Identification of the boundary between the shear sliding zone and the flexural toppling zone requires a more complex approach:

(1) Assume the boundary lies at the interface between column k-1 and column k (i.e., columns 1 to k-1 belong to the shear sliding zone).

(2) Calculate the maximum sustainable thrust P_k^s at the upper boundary of column k-1 by iterating upwards from column 1 to k-1 using the shear sliding zone equation, assuming $P_1^s = 0$ (toe condition):

$$P_{i+1}^s = \frac{1}{\lambda_i^s}(\kappa_i^s P_i^s - \varepsilon_i^s G_i + \mu_i^s T_i + c_i b_i) \quad (24)$$

(3) Calculate the maximum sustainable thrust at the upper boundary of column k under two competing failure mode assumptions: (a) shear sliding assumption for column k:

$$P_{k+1}^s = \frac{1}{\lambda_k^s}(\kappa_k^s P_k - \varepsilon_k^s G_k + \mu_k^s T_k + c_k b_k) \quad (25)$$

and (b) flexural toppling assumption for column k:

$$P_{k+1}^t = \frac{1}{\lambda_k^t}(\kappa_k^t P_k^s - \varepsilon_k^t G_k + \mu_k^t T_k + b_k^2\sigma_k^t) \quad (26)$$

(4) The actual failure mode of column k is determined by comparing the required thrust needed for stability against the maximum it can sustain under each mode. Column k will undergo flexural toppling if:

$$P_{k+1}^{t} < P_{k+1}^{s} \tag{27}$$

(5) Boundary identification: if condition (27) is true, columns 1 to *k*-1 constitute the shear sliding zone, and columns *k* to *n* belong to the flexural toppling and stable zones; if false, the assumed boundary *k* is too low; increment *k* and repeat steps 2-4 until condition (27) is satisfied.

3.3. Local Stability Assessment of Rock Columns

Accurate evaluation of local stability is paramount for implementing targeted and cost-effective slope protection measures. Engineers can optimize reinforcement design (e.g., bolt density, length, or localized grouting) based on spatial variations in stability revealed by this assessment. Traditional models for flexural toppling slope stability predominantly utilize the global FoS, which, while providing an intuitive measure of overall stability, fails to capture the inherent spatial heterogeneity and localized failure characteristic of anti-dip slope. To overcome this limitation, this study introduces a significant methodological advancement.

A novel Factor of Local Safety (FoLS) metric is introduced for quantifying the stability of individual rock columns within anchored anti-dip slopes. FoLS for column *j* is defined as the ratio of its total resisting force (R_j) to its total driving force (D_j):

$$FoLS_j = \frac{R_j}{D_j} \tag{28}$$

For $FoLS_j \geq 1.0$, column *j* is stable, and higher values indicate greater stability margins; for $0 < FoLS_j < 1.0$, column *j* is unstable (failed). Computing *FoLS* for all columns requires zonal calculation of R_j and D_j based on the identified boundaries.

(i) Column *j* in the shear sliding zone ($1 \leq j < k$)

Based on the force equilibrium conditions (Equations 10 and 11), the resisting and driving forces are:

$$R_j = P_{j+1}^{u} \tan\varphi_j \tan\varphi'_{j+1} + P_j^{d} + G_j \sin\alpha \tan\varphi_j + T_j/w_j\left[\sin(\alpha-\delta) + \cos(\alpha-\delta)\tan\varphi_j\right] \tag{29}$$

$$D_j = P_{j+1}^{u} + G_j \cos\alpha + P_j^{d} \tan\varphi'_j \tan\varphi_j \tag{30}$$

where P_j^{d} (thrust from column *j*-1 on *j*) and P_{j+1}^{u} (thrust from column *j*+1 on *j*) must be obtained iteratively.

(a) P_j^{d} Calculation: iterate upwards from *i*=2 to *i*=*j* using the shear sliding zone thrust Equation:

$$P_i^{d} = \frac{1}{\lambda_{i-1}^{s}}\left(\kappa_{i-1}^{s}P_{i-1}^{d} - \varepsilon_{i-1}^{s}G_{i-1} + \mu_{i-1}^{s}T_{i-1} + c_{i-1}b_{i-1}\right) \tag{31}$$

Note that if calculated $P_i^{d} < 0$, set $P_i^{d} = 0$ (no tensile capacity at interfaces). This applies to all thrust calculations.

(b) P_{j+1}^{u} Calculation: iterate downwards using appropriate equations above and below *k*. Firstly, iterate *i* from *n*-1 down to *k* using the toppling zone thrust equation, to find P_k^{u}:

$$P_{i+1}^{u} = \frac{1}{\kappa_{i+1}^{t}}(\lambda_{i+1}^{t}P_{i+2}^{u} + \varepsilon_{i+1}^{t}G_{i+1} - \mu_{i+1}^{t}T_{i+1} - b_{i+1}^{2}\sigma_{i+1}^{t}) \tag{32}$$

Secondly, iterate *i* from *k*-1 down to *j* using the shear sliding zone thrust equation to find P_{j+1}^{u}:

$$P_{i+1}^{u} = \frac{1}{\kappa_{i+1}^{s}}(\lambda_{i+1}^{s}P_{i+2}^{u} + \varepsilon_{i+1}^{s}G_{i+1} - \mu_{i+1}^{s}T_{i+1} - c_{i+1}b_{i+1}) \tag{33}$$

(ii) Column *j* in the toppling or stable zone ($k \leq j \leq n$)

Based on the moment equilibrium criterion (Equation 17), the resisting and driving forces are defined as:

$$R_j = 4P_{j+1}^{u}b_j \tan\varphi'_{j+1} + P_j^{d}\left(6\eta h_j + 3b_j \tan\varphi'_j\right) + G_j b_j \sin\alpha + T_j\left[6\bar{h}_j \sin(\alpha-\delta) + b_j\cos(\alpha-\delta)\right] + b_j^{2}\sigma_j^{t} \tag{34}$$

$$D_j = 6P_{j+1}^{u}\eta h'_j + 3G_j\bar{h}_j\cos\alpha + P_j^{d}b_j\tan\varphi'_j \tag{35}$$

Similarly, the thrust forces P_j^{d} and P_{j+1}^{u} are obtained iteratively.

(a) P_j^{d} Calculation: firstly, iterate *i* from 1 to *k*-1 using shear sliding thrust equation to find P_k^{d}:

$$P_i^{d} = \frac{1}{\lambda_{i-1}^{s}}\left(\kappa_{i-1}^{s}P_{i-1}^{d} - \varepsilon_{i-1}^{s}G_{i-1} + \mu_{i-1}^{s}T_{i-1} + c_{i-1}b_{i-1}\right) \tag{36}$$

Secondly, iterate i from k+1 to j using the toppling zone thrust equation to find P_j^d:

$$P_i^d = \frac{1}{\lambda_{i-1}^t}\left(\kappa_{i-1}^t P_{i-1}^d - \varepsilon_{i-1}^t G_{i-1} + \mu_{i-1}^t T_{i-1} + b_{i-1}^2 \sigma_{i-1}^t\right) \quad (37)$$

(b) P_{j+1}^u Calculation: iterate downwards from i=n-1 to i=j using the toppling zone thrust Equation:

$$P_{i+1}^u = \frac{1}{\kappa_{i+1}^t}\left(\lambda_{i+1}^t P_{i+2}^u + \varepsilon_{i+1}^t G_{i+1} - \mu_{i+1}^t T_{i+1} - b_{i+1}^2 \sigma_{i+1}^t\right) \quad (38)$$

This section develops an advanced mechanical framework for local stability assessment of anchored anti-dip slopes, introducing the novel FoLS metric. By integrating zonal partitioning, thrust force iteration algorithms, and failure mode-specific stability criteria, the model quantifies stability heterogeneity across slope profiles. This approach overcomes limitations of conventional global safety factors, enabling granular spatial assessment to optimize targeted reinforcement strategies for flexural toppling slopes.

4. Probabilistic Analysis of Spatiotemporal Stability Evolution

4.1. Monte Carlo Simulation-based Probabilistic Framework

While various methods exist for probabilistic slope stability analysis, Monte Carlo simulation (MCS) is particularly suited for this study due to its flexibility in handling complex functional relationships and diverse input parameter distributions [52, 53]. The MCS framework for evaluating the slope stability comprises four core stages: (a) define conditions - construct the slope stability state function and identify random variables with their probability distributions; (b) generate samples - generate a large number of possible parameter combination samples according to the distributions of the random variables; (c) deterministic calculation - for each sample parameter combination, perform a deterministic slope stability calculation to obtain the factor of safety; and (d) probabilistic stability evaluation - statistically analyze the probability density and distribution of the factor of safety and compute the failure probability.

For an anchored anti-dip slope comprising n rock columns, the FoLS at column j, time t, and for sample r is expressed as:

$$FoLS_j^{(r)}(t) = \frac{R_j^{(r)}(t)}{D_i^{(r)}(t)} = g_j\left[\chi_1^{(r)}, \chi_2^{(r)}, \ldots, \chi_n^{(r)}, j, t\right] \quad (39)$$

where, $g(x)$ is the state function for FoLS, and χ is the vector of physical property parameters for the slope-anchorage system, i.e., $\chi_i^{(r)} = \left[\gamma_i^{(r)}, \varphi_i^{(r)}, f_{si}^{(r)} \ldots\right]$.

Based on the MCS results, statistical analysis can be performed on the calculated FoLS values for each column. The probability density function (PDF) for column j is:

$$f_j(y) = \frac{1}{m \cdot \Delta y}\left\{\sum_{r=1}^{m} J\left\{y + \Delta y - g_j\left[\chi_1^{(r)}, \chi_2^{(r)}, \ldots, \chi_n^{(r)}, j, t\right]\right\} - \sum_{r=1}^{m} J\left\{y - g_j\left[\chi_1^{(r)}, \chi_2^{(r)}, \ldots, \chi_n^{(r)}, j, t\right]\right\}\right\} \quad (40)$$

where, $J(x)$ is the indicator function, defined as:

$$J(x) = \begin{cases} 0 & \text{for} \quad x \le 0 \\ 1 & \text{for} \quad x > 0 \end{cases} \quad (41)$$

The corresponding cumulative distribution function (CDF) is:

$$F_j(y) = \frac{1}{m}\sum_{r=1}^{m} J\left\{y - g_j\left[\chi_1^{(r)}, \chi_2^{(r)}, \ldots, \chi_n^{(r)}, j, t\right]\right\} \quad (42)$$

Local failure probability (P^f) for column j at time t is defined as the probability that $FoLS_j < 1$, derived directly from the CDF:

$$P_j^f = F_j(1) = \frac{1}{m}\sum_{r=1}^{m} J\{1 - g_j[\chi_1(r), \chi_2(r), \ldots, \chi_n(r)]\} \quad (43)$$

4.2. Computational Procedure for Spatiotemporal Evolution

The probabilistic framework described above is implemented computationally through a sequential, algorithmic procedure that integrates the deterministic mechanical model with stochastic inputs and MCS. The detailed logic and data flow of this procedure are illustrated in the algorithm flowchart presented in Figure 5. The core computational sequence is as follows:

(1) Initialization and sampling: define the geometric configuration of the anti-dip slope; for each random physical parameter, generate $m \times n$ sample realizations consistent with their assigned probability distributions.

(2) Corrosion modeling and bolt capacity degradation: For each bolt and sample r, compute corrosion depth Δd at time t using Equation 2; calculate degradation parameters α_s, η_s, and r_{bg} via Equations 4, 5, and 7; determine time-

dependent bolt tensile capacities T_a, T_b, and T_c under yield, bolt-grout bond, and grout-rock bond failure modes using Equations 3, 6, and 8; compute the system tensile capacity T as minimum among T_a, T_b, and T_c (Equation 9).

(3) Stability parameter calculation: calculate coefficients λ_i^s, κ_i^s, ε_i^s, and μ_i^s for the shear sliding zone using Equations 13 to 16; calculate coefficients λ_i^t, κ_i^t, ε_i^t, and μ_i^t for the flexural toppling zone using Equations 20 to 23.

(4) Zone boundary identification: employ the iterative procedure (Equations 24 to 27) to identify the sliding-toppling boundary (Column k) for each sample r.

(5) Inter-column thrust calculation: for each column j and sample r, compute thrust forces P_j^d and P_{j+1}^u: using Equations 31 to 33 for $1 \leq j < k$ and Equations 36 to 38 for $1 < j \leq n$.

(6) Local safety factor (FoLS) computation: for each column j and sample r, calculate resisting force $R_j^{(r)}$ and driving force $D_j^{(r)}$: using Equations 29 to 30 for $1 \leq j < k$ and Equations 34 to 35 for $1 < j \leq n$; compute $FoLS_j^{(r)} = R_j^{(r)}/D_j^{(r)}$.

(7) Probabilistic post-processing: for each column j and time t, construct PDF (Equation 40) and CDF (Equation 42) from the m sets of $FoLS_j$ values; compute local failure probabilities P_j^f (Equation 43); analyze the evolution of CDF, PDF and P_j^f across the slope profile and over bolt service time to characterize spatiotemporal stability degradation.

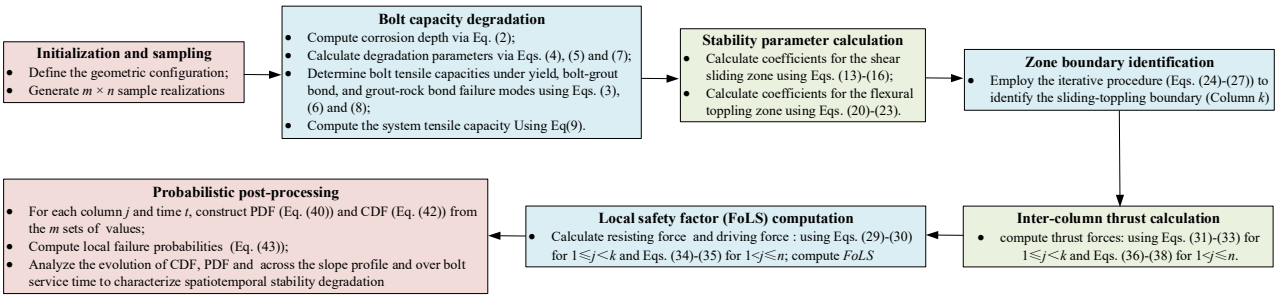

Figure 5. Flowchart of the computational procedure

5. Results

5.1. Illustrative Case

A representative anchored anti-dip slope with a height of 40.8 m serves to validate the proposed spatiotemporal probabilistic model. The slope exhibits rock strata dipping at 60°, and the slope face comprises three benches with a crest inclination of 3° and bench-face inclinations of 69°. The potential failure surface dips at 38°, intersecting bedrock where six rows of bolts per bench are installed with vertical and horizontal spacings of 2.4 m and 3.0 m respectively, inclined at 15°, and fully bonded in stable strata (Figure 6). Stochastic parameters governing the slope-anchorage system, detailed in Table 1, assign probability distributions—normal for dimensional parameters (d_0, D_0, L_b, L_c) and lognormal for strength parameters (γ, φ, φ', σ^t, f_s, τ_{bg}, τ_{gr}, r_{wc})—with specified means, standard deviations, and coefficients of variation (COV). Implementing the Monte Carlo framework in MATLAB, 100,000 stochastic realizations were generated for each of the 113 columns to compute the Factor of Local Safety (FoLS) across a 200-year service horizon, capturing comprehensive stability evolution.

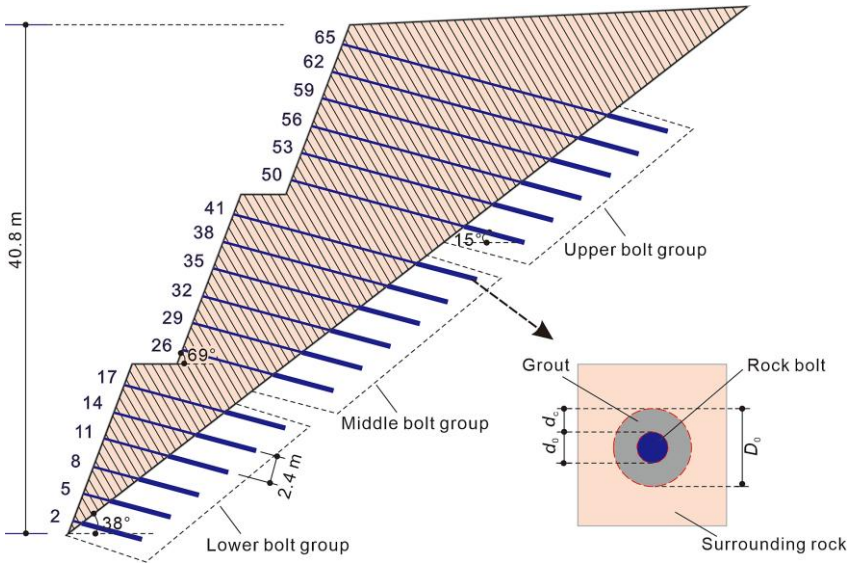

Figure 6. Geometry and anchorage configuration of the case study slope

Table 1. Physical parameters for slope-anchorage system of the study case

Parameter	Distribution	Mean	St. Dev.	COV
γ (kN/m^3)	Normal	26.5	5.3	0.2
φ (°)	Lognormal	40	8.0	0.2
φ' (°)	Lognormal	28	11.2	0.4
σ^t (kPa)	Lognormal	1000	400	0.4
d_0 (mm)	Normal	36	0.36	0.01
D_0 (mm)	Normal	120	12	0.1
L_b (m)	Normal	5	0.5	0.1
L_c (m)	Normal	5	0.5	0.1
f_a (MPa)	Lognormal	500	5.0	0.01
τ_b (kPa)	Lognormal	1000	150	0.15
τ_c (kPa)	Lognormal	500	200	0.4
r_{wc}	Lognormal	0.5	0.05	0.1

5.2. Statistical Characterization of FoLS Distributions

Probability density functions (PDFs) for 10 representative columns reveal position-dependent morphologies that evolve over time (Figure 7). Spatially, lower columns (excluding the very bottom) exhibit unimodal distributions with steep ascending and descending limbs. Mid-slope columns show broader unimodal distributions featuring flattened pre-peak slopes. Upper columns develop pronounced bimodality after 50 years of service: a primary peak at FoLS≈2.0 (indicating partial bolt degradation) and a secondary peak at FoLS≈40-80 (reflecting intact anchorage), arising from nonlinear interactions between parameter variability and corrosion-induced strength reduction. Temporally, the probability density curves shift leftward with increasing bolt service time. Additionally, for lower and mid-slope columns, the PDF peaks become higher and sharper through a smooth evolutionary process. For upper columns, the right peak (higher FoLS values) diminishes while the left peak (lower FoLS values) increases, indicating a sudden failure transition from high FoLS to low FoLS regimes.

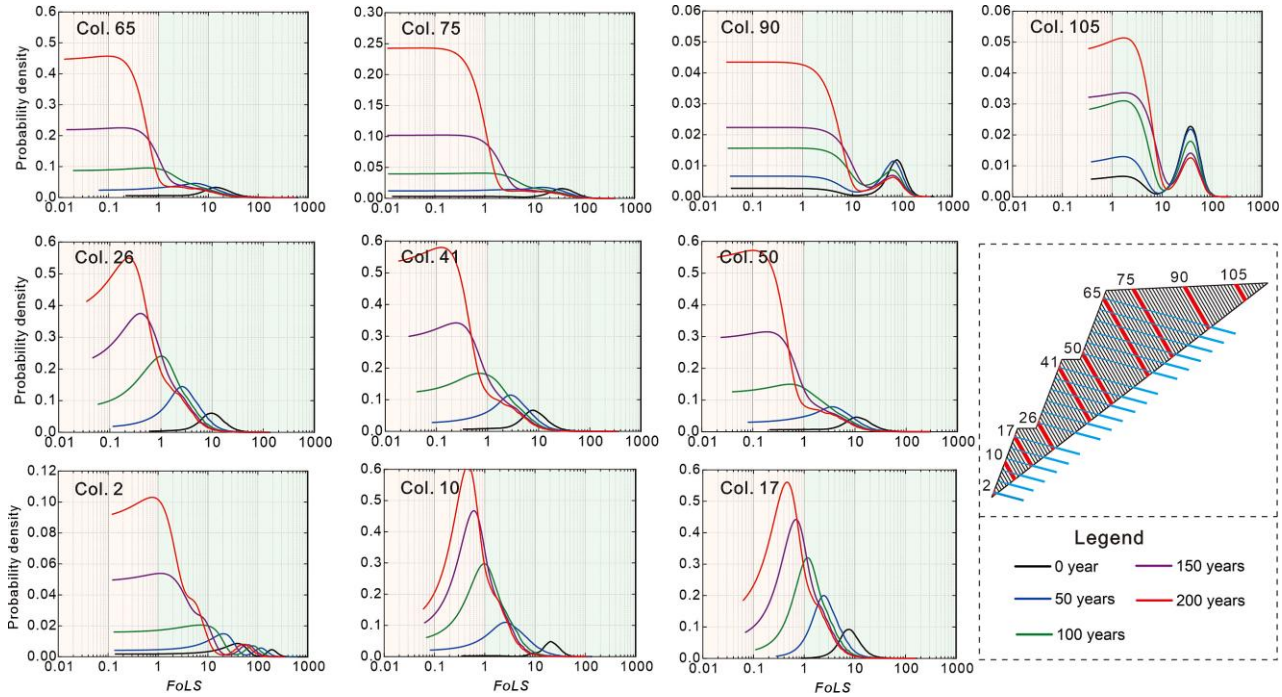

Figure 7. Spatiotemporal evolution of FoLS probability density

Cumulative distribution functions (CDFs, Figure 8) exhibit corresponding complexity: lower-column CDFs follow three-phase growth (gradual→steep→gradual), whereas mid/upper columns progress through five distinct phases. The latter initiates with gradual increase, accelerates steeply through the first PDF peak, moderates across the PDF valley, surges steeply through the second PDF peak, and finally plateaus . This five-stage progression, particularly the abrupt transition spanning FoLS from above 10 to below 1.0 in columns 67–110, signifies order-of-magnitude stability deterioration where local failure probability increases 3–5-fold within a single decade.

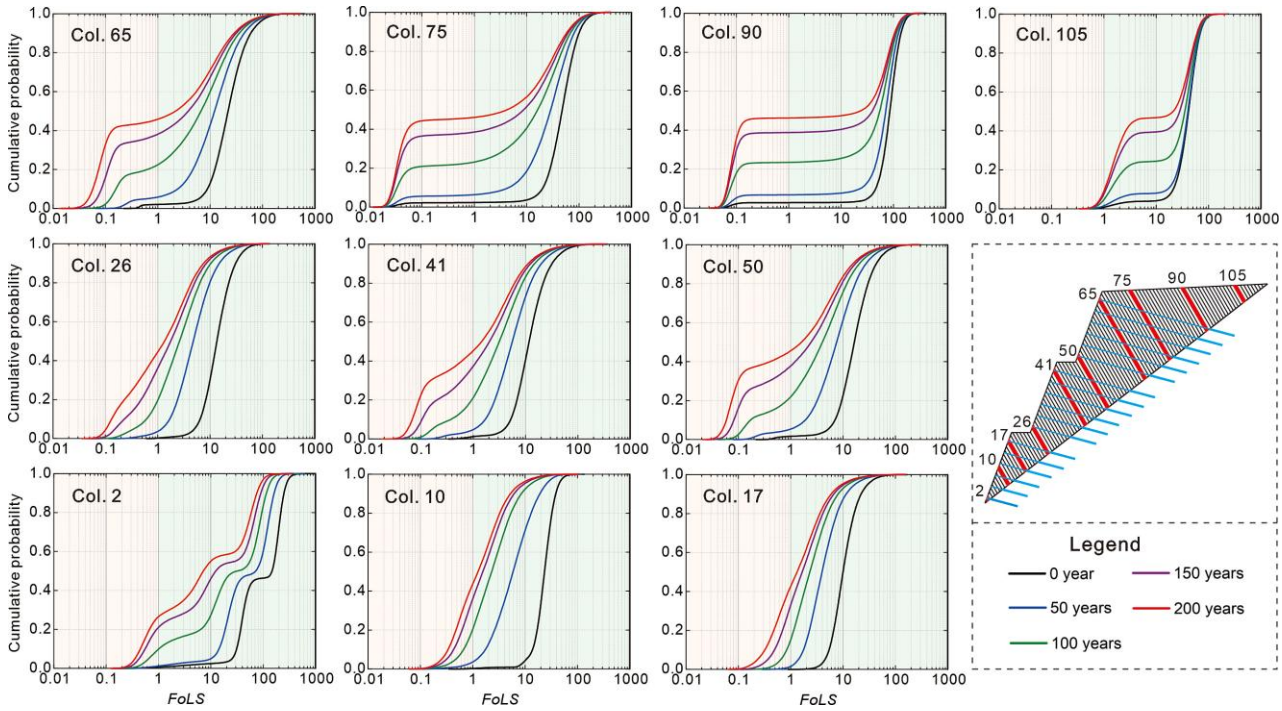

Figure 8. Spatiotemporal evolution of FoLS cumulative probability distributions

5.3. Spatiotemporal Evolution of FoLS Degradation

Figure 9 illustrates the three-dimensional spatiotemporal variation of the log-normalized mean FoLS, calculated using a logarithmic average over 100,000 simulations. Results for the unreinforced slope are provided as a baseline reference for comparative purposes. The main findings can be summarized as follows: (a) The anchored slope displays a spatial distribution of FoLS marked by elevated stability at the slope toe and crest, and reduced values across the mid-slope region. While this pattern is consistent with that observed in unanchored slopes, the mid-slope rock columns in the anchored system exhibit substantially enhanced stability compared to the unreinforced case. (b) The FoLS exhibits a gradual decline with increasing bolt service time,

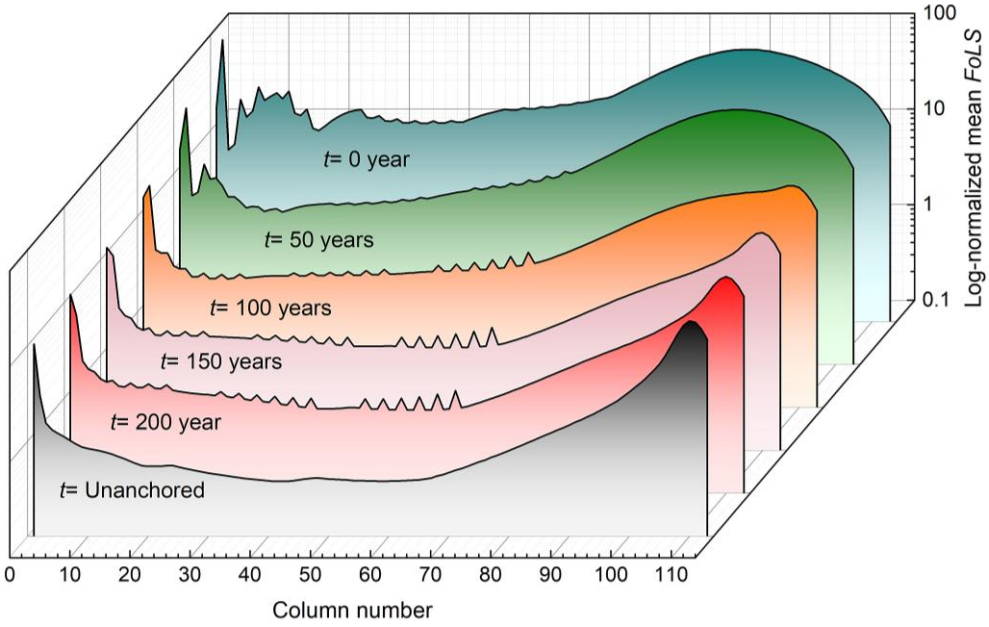

Figure 9. Spatiotemporal evolution of log-normalized mean FoLS

though the rate of reduction slows progressively. Notably, the upper-middle section of the slope (columns 67–110) experiences a rapid decrease in FoLS during the initial service period, followed by a more subdued reduction in later stages. This implies that failure initiates within this region and progressively extends toward the central and lower

portions of the slope as service time advances. (c) Pronounced serrated patterns are visible along the FoLS curves, aligning with the positions of rock columns where bolts are installed. These irregular features become increasingly conspicuous over extended service durations, highlighting the localized influence of corrosion on the performance of the anchorage system.

To visualize evolutionary trends and variability in the FoLS, Figure 10 displays log-normalized mean values and quantile distributions. As bolt service time increases, both the mean and quantile curves exhibit a gradual downward shift, revealing the following patterns: (a) During the initial service period, the curves display an upward convexity, which progressively evolves into a catenary form. This transition indicates that columns in the upper-middle slope region (67–110) undergo faster FoLS degradation compared to those in lower regions over time. (b) Initially, FoLS values show low dispersion, with the median curve closely aligning with the mean—suggesting a symmetric distribution. As service time advances, dispersion increases markedly, particularly in upper slope areas. Values below the 50th percentile exhibit substantially greater variability than those above, resulting in the mean curve falling below the median. (c) With prolonged service, both mean and quantile curves gradually converge toward the FoLS profiles characteristic of unanchored slopes, demonstrating asymptotic behavior under corrosion-induced degradation.

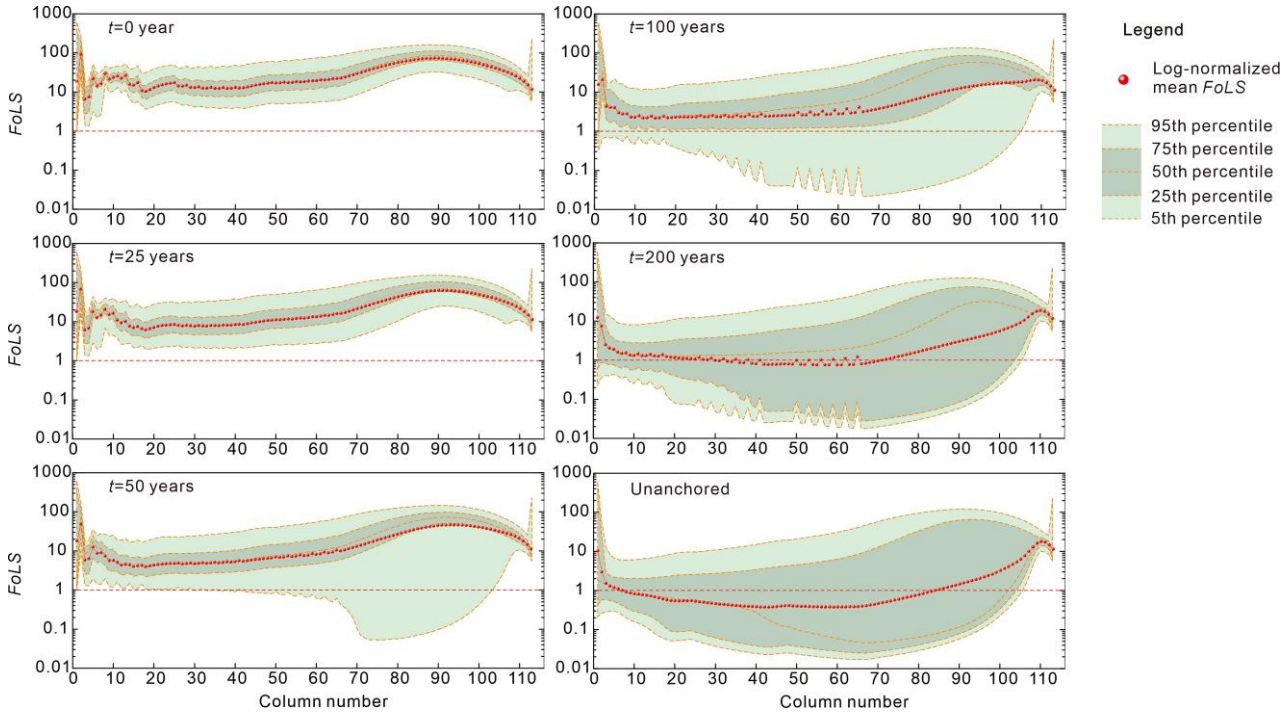

Figure 10. Temporal evolution of FoLS quantiles across column positions

5.4. Local Failure Probability Dynamics

Figure 11 presents the temporal evolution of the local failure probability across the slope profile. The key observations are summarized as follows: (a) The uppermost rock columns remain intact throughout the service period, showing no evidence of failure. The failure probabilities are significantly lower in the bottom columns than in the mid-slope regions. These probabilities increase sharply with elevation in the lower section, but eventually rise more moderately on the upper slope segments. (b) The failure probability progresses non-linearly over time, exhibiting three distinct phases: an initial stage of gradual increase, followed by a period of rapid acceleration, and a final phase marked by reduced growth rate. (c) While mid-slope columns (11–100) display consistent temporal trends in failure probability, notable positional differences are observed in both the bottom (1–10) and top (101–113) regions. Specifically, within the bottom region, columns situated at higher elevations (closer to the mid-slope) exhibit a more rapid increase in failure probability. Conversely, in the top region, columns located nearer to the slope crest demonstrate a slower progression of failure. (d) Rock columns restrained by anchor heads show markedly reduced failure probabilities compared to adjacent columns, leading to serrated profiles along the failure probability curves. These jagged features are particularly prominent in the lower anchor zones, mirroring the serration patterns observed in the logarithmically normalized mean FoLS curves.

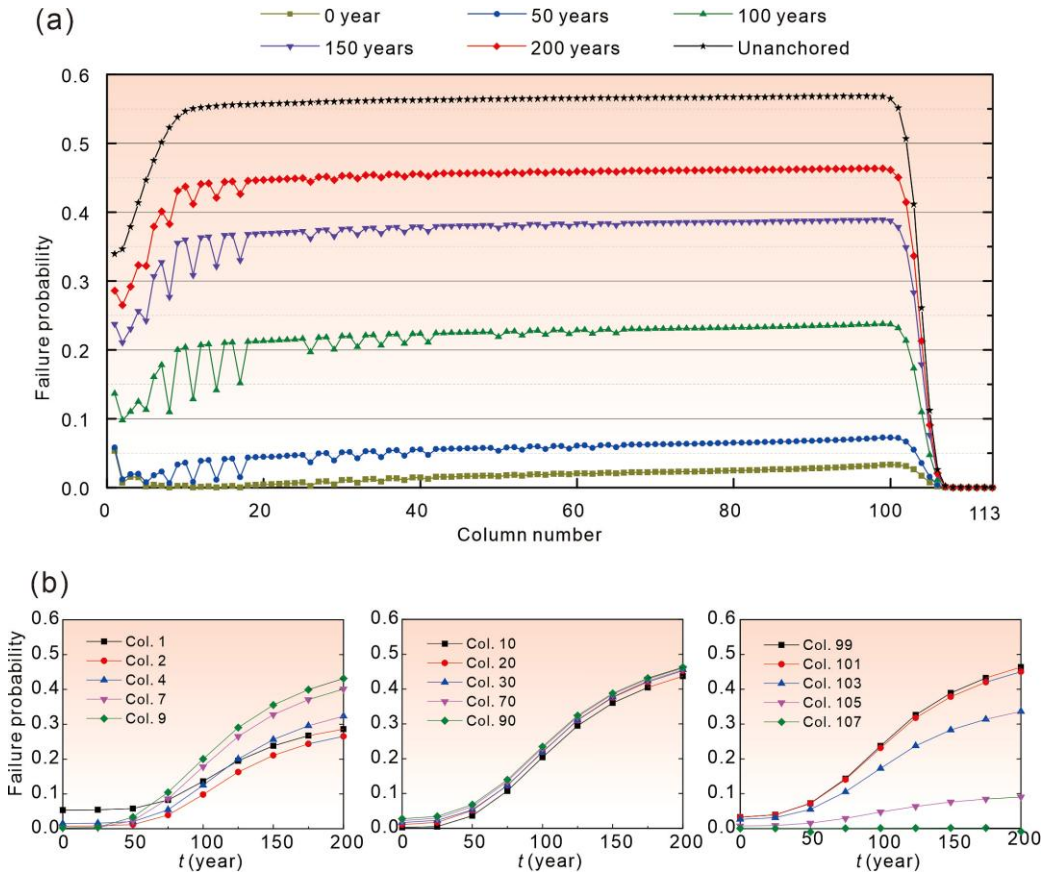

Figure 11. Spatiotemporal characteristics of local failure probability: (a) Spatial distribution; (b) Time-series evolution for critical columns

6. Discussion

6.1. Comparative Analysis with Global Factor of Safety

To explicitly address the limitations of conventional approaches and underscore the advantage of the proposed local stability metric, a comparative analysis was conducted. Using identical parameters and the same Monte Carlo simulation framework, the time-dependent global Factor of Safety (FoS) for the entire slope was computed alongside the mean FoLS for five representative columns (Columns 2, 17, 65, 90, and 105) over the 200-year service period. The comparative results are presented in Figure 12.

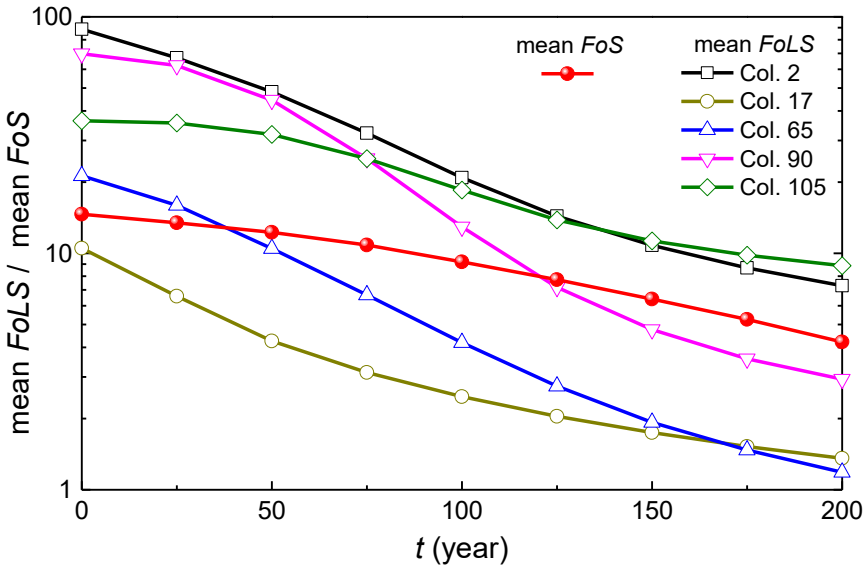

Figure 12. Comparison between the global Factor of Safety (FoS) and the Factor of Local Safety (FoLS) for representative columns over time

The mean global FoS exhibits a gradual monotonic decline with increasing bolt service time, quantitatively reflecting the overall degradation of slope stability due to progressive corrosion. This trend aligns with engineering intuition and prior studies focusing on system-level reliability [20, 42]. However, the global FoS, as a single aggregated metric, fails to reveal the critical spatial heterogeneity of stability loss. It provides no insight into where within the slope the stability is deteriorating most rapidly or which zones are becoming vulnerable first.

In contrast, the local FoLS profiles unveil a more complex and informative picture. While the FoLS for all selected columns also decreases over time, the rate and pattern of degradation vary significantly with column location. Notably, the FoLS for columns in the upper-middle slope region (e.g., Columns 65 and 90) decays at a markedly faster rate than the global FoS, especially during the first 0-100 years. This indicates that these specific columns enter a state of significantly reduced stability margin long before the global FoS suggests a critical condition. Conversely, columns near the toe (Column 2) show a degradation rate more aligned with the global FoS. This spatial discrimination is precisely what the FoLS metric is designed to capture.

The comparison yields two key conclusions that affirm the advancement of the proposed framework. First, the traditional FoS approach has an inherent limitation in diagnosing localized, progressive failure mechanisms, as it averages stability across both stable and deteriorating zones. Second, the FoLS is a more sensitive and spatially resolved indicator. This granular insight is essential for the lifecycle management of extensive slope systems where failure initiates locally.

6.2. Parameter Sensitivity Analysis

We examined the effects of four critical parameters on the log-normalized mean FoLS and the failure probability of the anchored anti-dip slope: bolt inclination angle, bolt yield strength, bolt–rock interface bond strength, and grout water–cement ratio. All analyses assumed a bolt service life of 50 years, with other parameters held constant when assessing the influence of each individual variable. Results are presented for representative rock columns across the slope profile. Key observations from Figure 13 are summarized as follows:

(a) Bolt inclination angle: FoLS values decrease throughout the slope as the bolt inclination angle increases. Concurrently, local failure probabilities rise with larger angles.

(b) Bolt yield strength: When the bolt strength is below 300 MPa, FoLS increases with higher strength but stabilizes beyond 300 MPa. Failure probability declines with increasing strength up to 300 MPa and remains nearly constant thereafter.

(c) Bolt-rock bond strength: FoLS exhibits a strong positive correlation with bond strength, showing rapid improvement at higher values. Local failure probability decreases accordingly.

(d) Water–cement ratio: FoLS is highly sensitive to the water–cement ratio, decreasing at a progressively increasing rate as the ratio rises. Failure probability shows a marked increase with higher water–cement ratios.

Additionally, Column 90 demonstrates greater sensitivity to parameter variations compared to other locations. This heightened sensitivity may be attributed to its position near the sub-critical boundary of the active toppling zone: stability improves progressively above this column, whereas it deteriorates gradually below it.

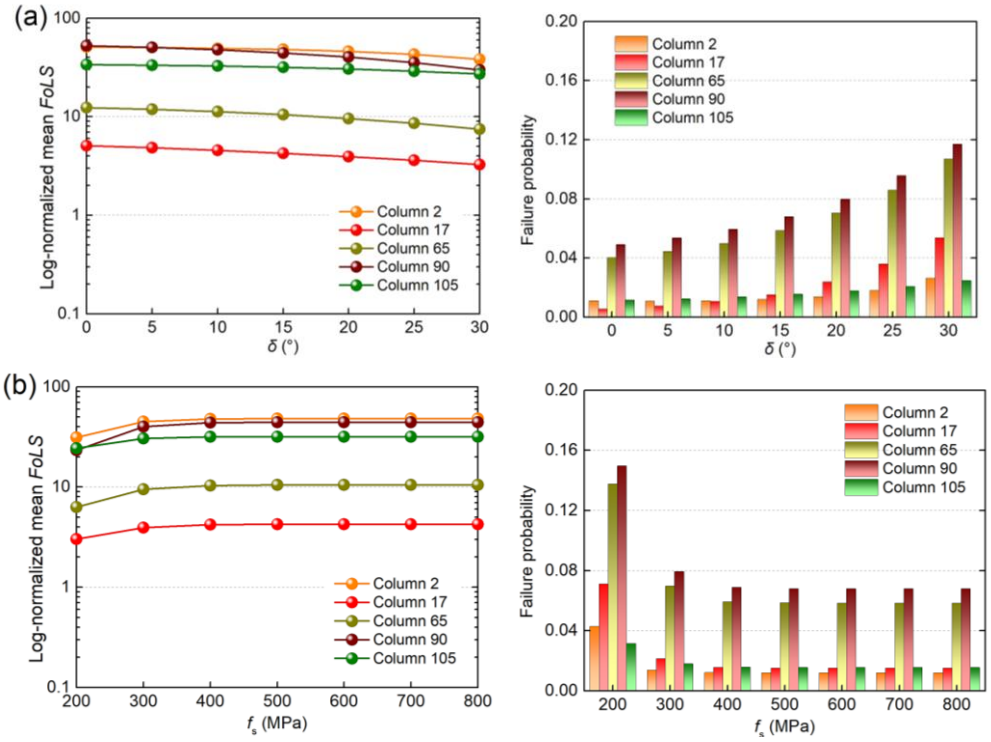

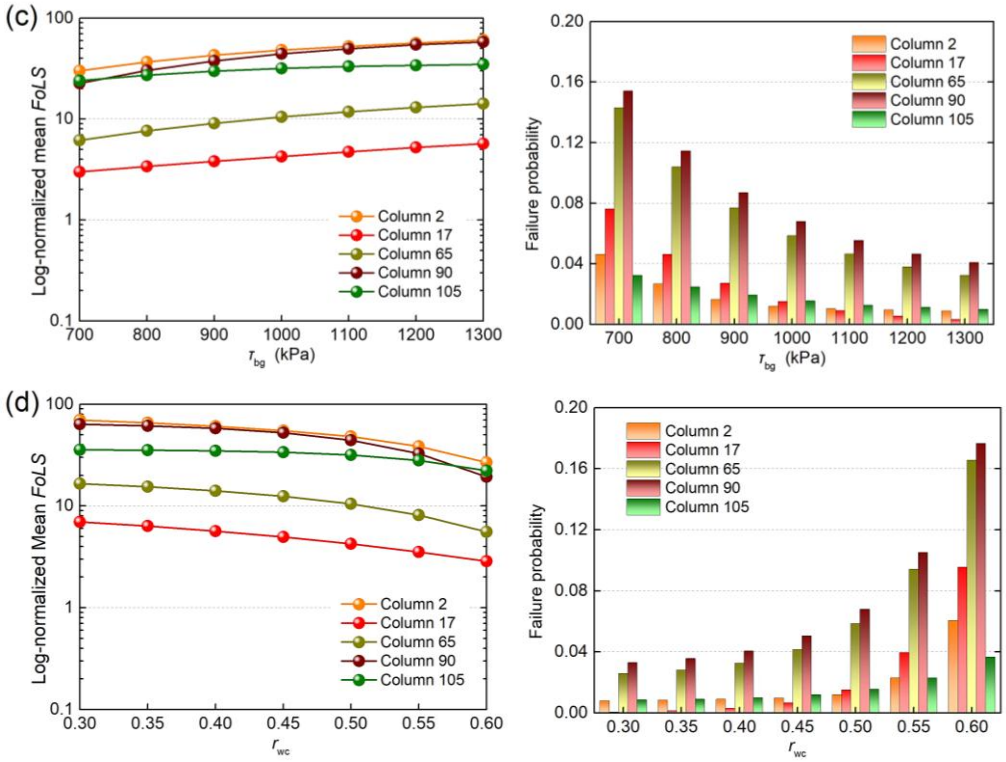

Figure 13. Parametric influence on log-normalized mean FoLS and local failure probability after 50-year service: (a) Bolt inclination angle; (b) Bolt yield strength; (c) Bolt-rock bond strength; (d) Grout water-cement ratio

6.3. Anchorage Effectiveness at Different Slope Positions

The case study examines a slope stabilized with a three-bench anchorage system. To evaluate the effectiveness of anchoring at specific bench locations, three partial anchorage scenarios were investigated: anchoring only the lower bench, only the middle bench, or only the upper bench. The log-normalized mean FoLS for each configuration was compared with both the fully anchored condition (all three benches reinforced) and the unanchored baseline. Figure 14 presents the FoLS profiles at two critical time intervals: immediately after installation and after 100 years of bolt service.

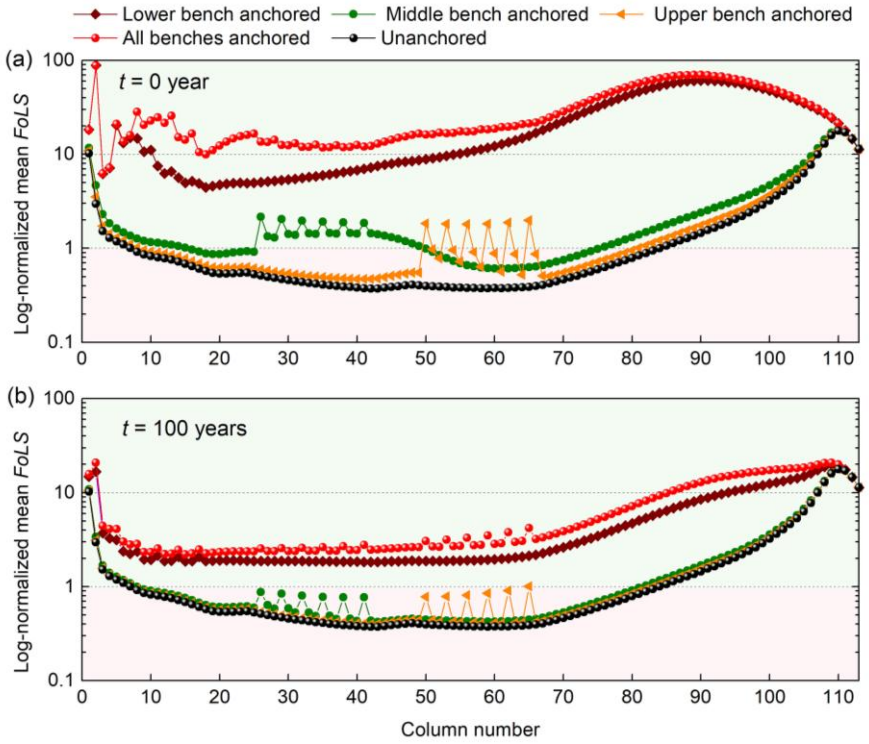

Figure 14. Anchorage configuration effects on log-normalized mean FoLS: (a) Initial installation; (b) After 100-year service

In the initial installation phase, lower-bench anchorage demonstrates superior stabilization performance, particularly for rock columns near the slope crest, outperforming both the middle-bench and upper-bench configurations. The lower-bench scenario achieves FoLS values comparable to those of the fully anchored condition in upper-slope regions. Anchorage at the middle bench provides moderate stabilization, significantly enhancing the stability of mid-slope columns (columns 25–65 in this study case). In contrast, upper-bench anchorage has a limited effect, with stability improvements confined mainly to the vicinity of the anchor heads and negligible influence elsewhere.

After 100 years of service, the FoLS curves for the middle- and upper-bench anchorage configurations (excluding the anchor head columns) closely align with the unanchored case, indicating an almost complete loss of anchorage effectiveness. This degradation is attributed to corrosion-induced failure within the rock-bolt systems in the upper and middle benches. In comparison, lower-bench anchorage maintains significantly better long-term performance, with FoLS values only slightly below those of the fully anchored slope, underscoring its reliability under prolonged corrosive conditions.

6.4. Corrosion-Induced Failure Mechanisms

The long-term stability of anchored anti-dip slopes is fundamentally governed by the progressive deterioration of the rock-bolt systems under corrosive environments. Through probabilistic spatiotemporal evolution analysis, this study elucidates a refined mechanism of failure that accounts for both the temporal degradation of bolt capacity and the spatial redistribution of forces within the slope. The slope profile is conceptually divided into three primary zones: the stable zone, the flexural toppling zone, and the shear sliding zone. Furthermore, the toppling zone can be subdivided into three distinct sub-zones based on kinematic activity and stress state: the moderately active toppling zone, the extremely active toppling zone, and the passive toppling zone (Figure 15). The failure process under continuous corrosion unfolds through the following progressive stages:

(1) Initial stability phase: Immediately upon installation, the rock-bolt systems operate at their full design capacity. Corrosion is negligible, and the slope exhibits maximum stability. The anchorage effectively restrains the toppling and shear tendencies, with force transfer occurring optimally through the bonded lengths into the stable bedrock.

(2) Onset of damage: Environmental exposure initiates measurable corrosion, particularly in the bolt heads and free lengths. This leads to a gradual reduction in the cross-sectional area and yield strength of the bolts, as well as a decline in the bond strength at the bolt-grout interface. Although the overall slope remains stable, the loss of tensile capacity becomes non-negligible. Micro-fractures and initial damage begin to accumulate within the extremely active toppling zone, where bending moments and tensile stresses are highest.

(3) Active deterioration phase: Corrosion progresses significantly, leading to a substantial decline in the load-bearing capacity of multiple rock-bolt systems. The extremely active toppling zone experiences widespread failure due to the combined effects of reduced bolt capacity and sustained flexural loading. This failure redistributes additional thrust forces downward and upward, initiating damage in the moderately active toppling zone. Simultaneously, the passive toppling zone is subjected to considerably increased thrust from the overlying unstable columns, leading to incipient shear and tensile damage.

(4) Advanced Failure Stage: Severe corrosion results in the functional failure of most rock-bolt structures in the upper and middle benches. The loss of confinement allows the moderately active toppling zone to undergo large deformations, further amplifying thrust forces acting on the passive zone. The accumulated thrust from the upper sections eventually exceeds the residual resistance of the passive toppling zone, resulting in its collapse. This phase is characterized by a sharp decline in the global stability reserve and the emergence through the slope face.

(5) Final Collapse: Ultimately, the entire rock-bolt system becomes severely corroded and incapable of sustaining any meaningful tensile loads. The failure propagates from the passive toppling zone into the shear sliding zone near the slope toe, leading to overall slope instability. It is noteworthy that the rock columns within the crest-stable zone remain largely unaffected throughout the entire process, underscoring the localized yet progressive nature of corrosion-induced failure.

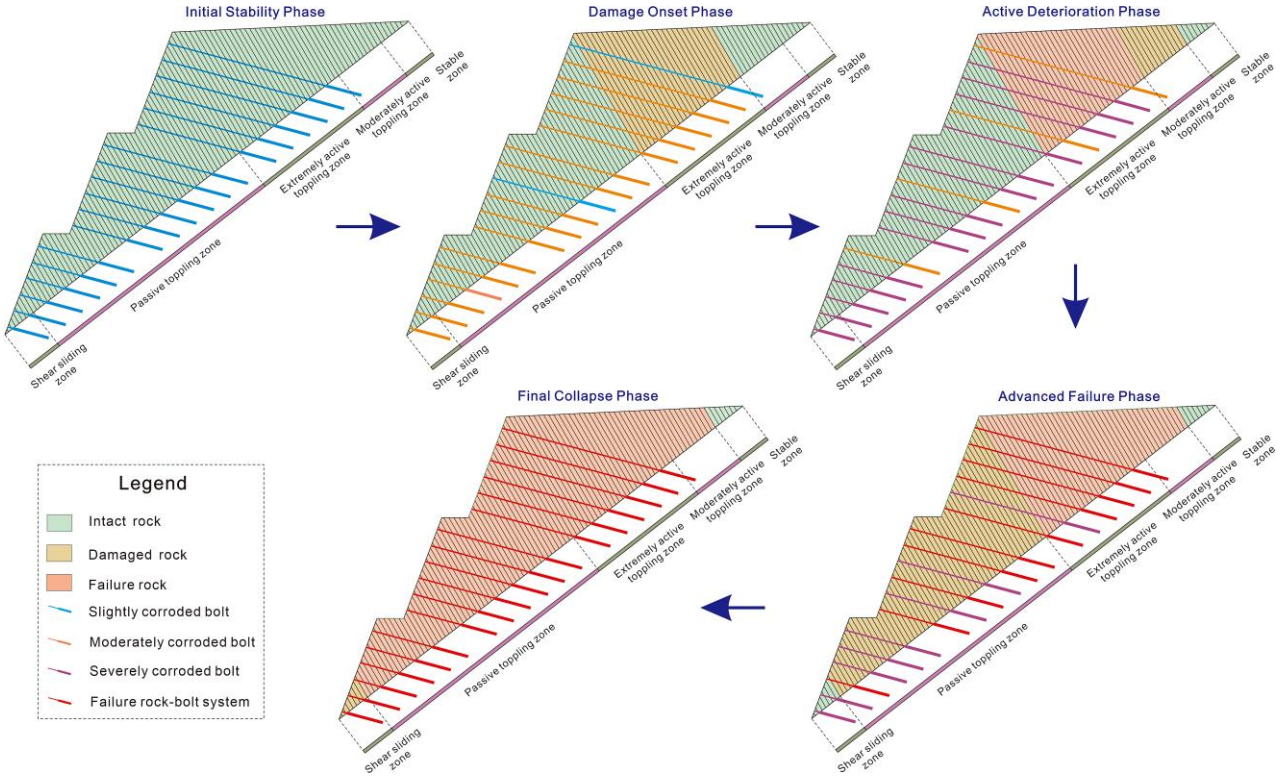

Figure 15. Corrosion-driven failure mechanism of anchored anti-dip slope

This proposed mechanism highlights the critical role of spatiotemporal corrosion progression in altering the internal force distribution and failure sequence of anchored anti-dip slopes. The integration of time-dependent bolt degradation with mechanical zone partitioning provides a comprehensive explanation for the observed evolutionary failure patterns, offering valuable insights for the design of monitoring systems and targeted reinforcement strategies.

6.5. Engineering Implications and Model Limitations

Based on mechanistic analyses and computational results presented in this study, the following optimization strategies are proposed for anti-dip slope anchoring engineering:

- Spatial arrangement optimization: Since rock-bolt systems in the upper slope endure higher tensile forces and are more susceptible to failure, anchor layout density in these regions should be increased, or the ultimate tensile capacity of individual bolts should be enhanced to improve overall anchorage performance. Bolt inclination angles should be oriented as horizontally as possible to maximize the anchorage efficiency of each bolt.
- Material design considerations: Bolt-rock bond strength has a greater influence on tensile capacity than bolt yield strength during bolt service. Design principle should therefore focus on improving interfacial adhesion through techniques such as surface roughening and extended anchor lengths. Additionally, lower grout water-cement ratios are recommended to reduce bolt corrosion rates.
- Dynamic assessment recommendations: As bolt service time increases, emphasis should shift from evaluating local failure probabilities to monitoring the spatial distributions of FoLS. In later phases, FoLS distributions exhibit significant dispersion—particularly in middle and upper slope regions—indicating a potential for sudden failure transitions.

The proposed model also has several limitations:

- The mechanical model simplifies rock bolt support as a concentrated tensile force at the column top. This neglects shear transfer and bending along the free length, especially in fully grouted bolts, potentially overestimating local stabilizing efficiency. Future incorporation of distributed load-transfer models would improve mechanical accuracy.
- The model incorporates two key simplifying assumptions for corrosion prediction: uniform radial corrosion, which reflects average degradation rates, and constant environmental conditions. In practice, however, localized pitting corrosion can induce earlier and more brittle bolt failure, while wet–dry cycles driven by seasonal or reservoir fluctuations generally accelerate corrosion. Future studies should integrate stochastic pitting models and transient environmental conditions to support more realistic and critical assessments.
- This study models bolt corrosion as the key degradation mechanism, neglecting potential long-term deterioration of grout or the grout-rock interface. In aggressive environments, such degradation would further reduce system

capacity, leading to more conservative stability predictions. This represents a critical area for future model development.

- Corrosion rate and bond strength evaluations in this study focus exclusively on bolts, omitting prestressed anchor cables commonly used in high-steep slope engineering. The corrosion mechanisms of prestressed anchor cables differ substantially from those of conventional bolts and warrant dedicated investigation.

7. Conclusions

This study developed an integrated probabilistic framework to evaluate the spatiotemporal stability evolution of anchored anti-dip slopes subjected to bolt corrosion, a critical issue for the long-term safety of hydropower reservoir slopes and mine high-walls. The main contributions and findings are summarized as follows:

- A time-dependent mechanical model was established to quantify the degradation of bolt tensile capacity under three failure modes, incorporating corrosion kinetics and bond strength reduction. This model effectively captures the progressive strength loss of support systems in aggressive environments.
- A novel Factor of Local Safety (FoLS) was proposed to assess the stability of individual rock columns, enabling spatially explicit stability evaluation. Coupled with an iterative thrust force algorithm and zonal boundary identification, FoLS overcomes the limitations of global safety factors and provides a powerful tool for identifying critical zones in extensive slope systems.
- Monte Carlo Simulation was employed to propagate uncertainties in material and geometric parameters, generating probabilistic distributions of FoLS and local failure probabilities over a 200-year service period. The results revealed complex spatiotemporal patterns, including bimodal FoLS distributions in upper columns and serrated stability profiles aligned with bolt positions.
- Case study analysis demonstrated that corrosion-induced stability degradation initiates in the upper-middle slope region and progressively propagates downward. Lower-bench anchorage proved most effective for long-term stability, while upper and middle benches exhibited significant performance loss after 100 years due to corrosion.
- Sensitivity analysis identified bolt inclination, yield strength, bolt-rock bond strength, and grout water-cement ratio as critical parameters influencing stability. Columns near sub-critical toppling boundaries showed heightened sensitivity to parameter variations.
- A refined failure mechanism was proposed, subdividing the toppling zone into extremely active, moderately active, and passive subzones. The failure propagates sequentially from the extremely active zone to the passive and shear sliding zones, elucidating the spatiotemporal progression of corrosion-driven slope instability.
- Practical recommendations were provided for optimizing anchorage design, including spatially differentiated bolt layouts, minimized bolt inclination, enhanced interfacial bond strength, and the use of low water-cement ratio grout.
- The proposed framework offers a robust, spatially resolved tool for the probabilistic assessment and lifecycle management of anchored anti-dip slopes in hydropower and mining engineering. Future work should incorporate bolt-grout interaction mechanics and extend the model to prestressed anchor cables widely used in high-steep slopes.

8. Declarations

8.1. Author Contributions

Conceptualization, D.J.W. and F.O.; methodology, D.J.W.; software, D.J.W. and Q.Y.W.; validation, Z.Q.F., F.O., and Y.H.Z.; writing—original draft preparation, D.J.W., Q.Y.W., and Z.Q.F.; writing—review and editing, F.O. and Y.H.Z.; supervision, F.O.; funding acquisition, D.J.W. and Y.H.Z. All authors have read and agreed to the published version of the manuscript.

8.2. Data Availability Statement

The data presented in this study are available on request from the corresponding author.

8.3. Funding

This research was funded by the National Natural Science Foundation of China (NSFC) (Grant No. 42307223), Hubei Natural Science Foundation (Grant No. JCZRQNB202600656), Scientific Research Plan of Hubei Provincial Department of Education (Grant No. Q20243001), Scientific Research Foundation of Hubei University of Education for Talent Introduction (Grant No. ESRC20240038), and Research Foundation of Anhui Provincial Intelligent Underground Detection and Geoenvironmental Engineering Research Center (Grant No. APIUDGERC2505).

8.4. Conflicts of Interest

The authors declare no conflict of interest.

9. References

[1] Goodman, R. E., & Kieffer, D. S. (2000). Behavior of Rock in Slopes. Journal of Geotechnical and Geoenvironmental Engineering, 126(8), 675–684. doi:10.1061/(asce)1090-0241(2000)126:8(675).

[2] Wyllie, D. C. (2017). Rock Slope Engineering. CRC Press, Boca Raton, United States. doi:10.4324/9781315154039.

[3] Huang, D., Ma, H., & Huang, R. (2022). Deep-seated toppling deformations of rock slopes in western China. Landslides, 19(4), 809–827. doi:10.1007/s10346-021-01829-9.

[4] Cheng, Y. G. (2012). Slope Anchoring Technology in China: State of the Art Report and its Prospect. Applied Mechanics and Materials, 256–259, 26–33. doi:10.4028/www.scientific.net/AMM.256-259.26.

[5] Li, B., Li, T., Xu, N., Dai, F., Chen, W., & Tan, Y. (2018). Stability assessment of the left bank slope of the Baihetan Hydropower Station, Southwest China. International Journal of Rock Mechanics and Mining Sciences, 104, 34–44. doi:10.1016/j.ijrmms.2018.02.016.

[6] Li, D. Q., Jiang, S. H., Cao, Z. J., Zhou, C. B., Li, X. Y., & Zhang, L. M. (2015). Efficient 3-D reliability analysis of the 530m high abutment slope at Jinping I Hydropower Station during construction. Engineering Geology, 195, 269–281. doi:10.1016/j.enggeo.2015.06.007.

[7] Yang, Y. X., Luo, G., Duan, Y. Y., Zhang, C. Z., Zhang, Y. G., & Lei, Q. (2020). Failure Mechanisms and Mitigation Measures of the G1006 Electricity Pylon Landslide in the Dam Area of the Jinping I Hydropower Station. IOP Conference Series: Earth and Environmental Science, 570(2), 022007. doi:10.1088/1755-1315/570/2/022007.

[8] Wu, S., Wang, L., Wu, Q., Tian, J., Zhu, L., Sun, Z., Zheng, L., & Wang, C. (2024). Dynamic stability analysis of anchored anti-dip slope under the Ludian earthquake: a case study of the Manhekuan slope, Yunnan, China. Bulletin of Engineering Geology and the Environment, 83(11), 429. doi:10.1007/s10064-024-03904-6.

[9] Wang, Y., Sun, X., & Ren, A. (2019). Investigations of rock anchor corrosion and its influence factors by exhumations in four typical field sites. Engineering Failure Analysis, 101, 357–382. doi:10.1016/j.engfailanal.2019.03.022.

[10] Yin, T., Sun, X., Wang, Y., & Zhao, Y. (2022). Corrosion Investigation of Rock Anchors Served over 10 Years in Underground Powerhouse of a Hydropower Station. Advances in Materials Science and Engineering, 4905010. doi:10.1155/2022/4905010.

[11] Yu, S., Lu, S., Hu, J., Guan, K., Wu, S., Liu, W., & Zhang, H. (2026). Combined Effect of Strain Rate and Corrosion on Bond Failure Mechanism of Rockbolt Grouted Structures. Rock Mechanics and Rock Engineering. doi:10.1007/s00603-025-05240-x.

[12] Yu, S., Lu, S., Wang, Y., Zhang, H., & Qi, F. (2025). Study on the deterioration of bond-slip performance of rockbolt grouted structures under corrosion. Computers and Geotechnics, 179, 106980. doi:10.1016/j.compgeo.2024.106980.

[13] Zheng, H., Jiang, Y., Wu, X., & Zhang, S. (2026). Shear performance degradation of bolted rock joint under corrosion-temperature coupling. Construction and Building Materials, 511, 145305. doi:10.1016/j.conbuildmat.2026.145305.

[14] Yang, Z., Xu, S., Wang, W., & Li, D. (2025). Experimental study on mechanical aging properties of self-swelling anchorage bolt under chemical corrosion. International Journal of Mining, Reclamation and Environment, 39(4), 309–324. doi:10.1080/17480930.2024.2393593.

[15] Li, Y., Zhang, S., Yang, R., & Shi, S. (2026). Investigation into the stress corrosion behavior of cable bolts under different tensile stresses. Tunnelling and Underground Space Technology, 171, 107452. doi:10.1016/j.tust.2026.107452.

[16] de Freitas, M. H., & Watters, R. J. (1974). Discussion: Some field examples of toppling failure. Géotechnique, 24(4), 691–693. doi:10.1680/geot.1974.24.4.691.

[17] Gu, D., & Huang, D. (2016). A complex rock topple-rock slide failure of an anaclinal rock slope in the Wu Gorge, Yangtze River, China. Engineering Geology, 208, 165–180. doi:10.1016/j.enggeo.2016.04.037.

[18] Zhu, C., He, M., Karakus, M., Cui, X., & Tao, Z. (2020). Investigating Toppling Failure Mechanism of Anti-dip Layered Slope due to Excavation by Physical Modelling. Rock Mechanics and Rock Engineering, 53(11), 5029–5050. doi:10.1007/s00603-020-02207-y.

[19] Zhao, Q., Yang, Z., Zhang, S., Gao, Y., Jin, X., Liu, X., & Li, B. (2025). Exploring the toppling deformation mechanisms and failure modes of anti-dip layered rocky slopes: insights from physical model experiments. Landslides, 22(3), 895–923. doi:10.1007/s10346-024-02405-7.

[20] Amini, M., Majdi, A., & Veshadi, M. A. (2012). Stability analysis of rock slopes against block-flexure toppling failure. Rock Mechanics and Rock Engineering, 45(4), 519–532. doi:10.1007/s00603-012-0220-7.

[21] Alejano, L. R., Sánchez-Alonso, C., Pérez-Rey, I., Arzúa, J., Alonso, E., González, J., Beltramone, L., & Ferrero, A. M. (2018). Block toppling stability in the case of rock blocks with rounded edges. Engineering Geology, 234, 192–203. doi:10.1016/j.enggeo.2018.01.010.

[22] Zhang, G., Wang, F., Zhang, H., Tang, H., Li, X., & Zhong, Y. (2018). New stability calculation method for rock slopes subject to flexural toppling failure. International Journal of Rock Mechanics and Mining Sciences, 106, 319–328. doi:10.1016/j.ijrmms.2018.04.016.

[23] Zheng, Y., Chen, C., Liu, T., Zhang, H., & Sun, C. (2019). Theoretical and numerical study on the block-flexure toppling failure of rock slopes. Engineering Geology, 263, 105309. doi:10.1016/j.enggeo.2019.105309.

[24] Ning, Y., Zhang, G., Tang, H., Shen, W., & Shen, P. (2019). Process Analysis of Toppling Failure on Anti-dip Rock Slopes Under Seismic Load in Southwest China. Rock Mechanics and Rock Engineering, 52(11), 4439–4455. doi:10.1007/s00603-019-01855-z.

[25] Zheng, X., Tao, Z., Shi, G., Yu, H., & He, M. (2025). The impact of groundwater level rise on toppling failure in anti-dip slopes: A physical model study. Bulletin of Engineering Geology and the Environment, 84(6), 330. doi:10.1007/s10064-025-04359-z.

[26] Cai, J., Zheng, D., Ju, N., Wang, J., Zhou, X., & Li, D. (2022). Time-Varying Effect of Ductile Flexural Toppling Failure on Antidip Layered Rock Slope. Frontiers in Earth Science, 10, 943700. doi:10.3389/feart.2022.943700.

[27] Mu, J., Li, T., Pei, X., Huang, R., Lan, F., & Zou, X. (2022). Evolution mechanism and deformation stability analysis of rock slope block toppling for early warnings. Natural Hazards, 114(2), 1171–1195. doi:10.1007/s11069-022-05422-8.

[28] Zhang, B., Ning, Y., Tang, H., Ding, B., Fang, K., & Zou, Z. (2023). Study on the evolutionary process of interbedded anti-inclined slope block-flexure toppling in the upper Yalong River. Bulletin of Engineering Geology and the Environment, 82(7), 240. doi:10.1007/s10064-023-03223-2.

[29] Sagaseta, C., Sánchez, J. M., & Cañizal, J. (2001). A general analytical solution for the required anchor force in rock slopes with toppling failure. International Journal of Rock Mechanics and Mining Sciences, 38(3), 421–435. doi:10.1016/S1365-1609(01)00011-9.

[30] Amini, M., Majdi, A., & Aydan, Ö. (2009). Stability analysis and the stabilisation of flexural toppling failure. Rock Mechanics and Rock Engineering, 42(5), 751–782. doi:10.1007/s00603-008-0020-2.

[31] Dong, M., Zhang, F., Lv, J., Hu, M., & Li, Z. (2020). Study on deformation and failure law of soft-hard rock interbedding toppling slope base on similar test. Bulletin of Engineering Geology and the Environment, 79(9), 4625–4637. doi:10.1007/s10064-020-01845-4.

[32] Tao, Z., Zhu, C., He, M., & Karakus, M. (2021). A physical modeling-based study on the control mechanisms of Negative Poisson's ratio anchor cable on the stratified toppling deformation of anti-inclined slopes. International Journal of Rock Mechanics and Mining Sciences, 138, 104632. doi:10.1016/j.ijrmms.2021.104632.

[33] Gong, W. J., Tao, Z. G., He, M. C., & Hou, H. J. (2022). Feasibility Analysis on the Support of Rock Slopes Against Flexural Toppling Failure Using the DDA Method-A Case Study. KSCE Journal of Civil Engineering, 26(9), 3847–3862. doi:10.1007/s12205-022-2331-3.

[34] An, X., Ju, G., & Bai, H. (2021). Study on simulation method of prestressed anchor cable reinforcement for large toppling slopes. 2021 7th International Conference on Hydraulic and Civil Engineering & Smart Water Conservancy and Intelligent Disaster Reduction Forum (ICHCE & SWIDR), 1463–1470. doi:10.1109/ICHCESWIDR54323.2021.9656489.

[35] Wu, S., Wang, L., Havenith, H. B., Tian, J., Wu, Q., Li, C., Ke, R., Wang, C., & Bi, X. (2025). Failure mechanism of anchored anti-dip rock slope subjected to strong earthquakes: Insights from large-scale shaking table tests. Engineering Geology, 355. doi:10.1016/j.enggeo.2025.108217.

[36] Sabatini, P. J., Pass, D. G., & Bachus, R. C. (1999). Ground anchors and anchored systems. FHWA-IF-99-015, Office of Bridge Technology, Federal Highway Administration, Washington, United States.

[37] Park, J., Qiu, T., & Kim, Y. (2013). Field and Laboratory Investigation of Pullout Resistance of Steel Anchors in Rock. Journal of Geotechnical and Geoenvironmental Engineering, 139(12), 2219–2224. doi:10.1061/(asce)gt.1943-5606.0000953.

[38] Zheng, D., Liu, F., Ju, N., Frost, J. D., & Huang, R. (2016). Cyclic load testing of pre-stressed rock anchors for slope stabilization. Journal of Mountain Science, 13(1), 126–136. doi:10.1007/s11629-015-3605-8.

[39] Jiang, S. H., Li, D. Q., Zhang, L. M., & Zhou, C. B. (2014). Time-dependent system reliability of anchored rock slopes considering rock bolt corrosion effect. Engineering Geology, 175, 1–8. doi:10.1016/j.enggeo.2014.03.011.

[40] Li, X.-Y., Fan, Z.-B., Lu, T., Xiao, T., & Zhang, L.-M. (2018). A Resilience Model for Engineered Slopes Subject to Anchor Corrosion. KSCE Journal of Civil Engineering, 22(3), 887–895. doi:10.1007/s12205-018-1041-3.

[41] Fu, G., Deo, R., Ji, J., & Kodikara, J. (2021). Failure assessment of reinforced rock slopes subjected to bolt corrosion considering correlated multiple failure modes. Computers and Geotechnics, 132, 104029. doi:10.1016/j.compgeo.2021.104029.

[42] Vu, K. A. T., & Stewart, M. G. (2000). Structural reliability of concrete bridges including improved chloride-induced corrosion models. Structural Safety, 22(4), 313–333. doi:10.1016/S0167-4730(00)00018-7.

[43] Chen, G., Li, Z., & Gong, W. (2026). Stability Assessment of Bolt-Reinforced Rock Slopes Considering Corrosion Effects. International Journal of Geomechanics, 26(3), 4026014. doi:10.1061/ijgnai.gmeng-12297.

[44] Cheng, X. W. (2010). Time-Varying Reliability Analysis of Rock Slope Anchorage System and Computational Method. Master Thesis, Hunan University, Changsha, China. (In Chinese).

[45] Lin, H., Zhao, Y., Feng, P., Ye, H., Ozbolt, J., Jiang, C., & Yang, J. Q. (2019). State-of-the-art review on the bond properties of corroded reinforcing steel bar. Construction and Building Materials, 213, 216–233. doi:10.1016/j.conbuildmat.2019.04.077.

[46] Syll, A. S., & Kanakubo, T. (2022). Impact of Corrosion on the Bond Strength between Concrete and Rebar: A Systematic Review. Materials, 15(19), 7016. doi:10.3390/ma15197016.

[47] Bhargava, K., Ghosh, A. K., Mori, Y., & Ramanujam, S. (2007). Corrosion-induced bond strength degradation in reinforced concrete-Analytical and empirical models. Nuclear Engineering and Design, 237(11), 1140–1157. doi:10.1016/j.nucengdes.2007.01.010.

[48] Ma, Y., Zhang, J., Wang, L., & Liu, Y. (2013). Probabilistic prediction with Bayesian updating for strength degradation of RC bridge beams. Structural Safety, 44, 102–109. doi:10.1016/j.strusafe.2013.07.006.

[49] Yu, X. H., Dai, K. Y., & Li, Y. S. (2021). Variability in corrosion damage models and its effect on seismic collapse fragility of aging reinforced concrete frames. Construction and Building Materials, 295, 123654. doi:10.1016/j.conbuildmat.2021.123654.

[50] Guo, H. Y., Jiang, C., Gu, X. L., Dong, Y., & Zhang, W. P. (2023). Time-dependent reliability analysis of reinforced concrete beams considering marine environmental actions. Engineering Structures, 288, 116252. doi:10.1016/j.engstruct.2023.116252.

[51] Wang, D. J., Tang, H., Zhang, Y., & Shen, P. (2019). Local failure probability of the anti-dip slope susceptible to flexural toppling. Stochastic Environmental Research and Risk Assessment, 33(4–6), 1187–1202. doi:10.1007/s00477-019-01683-1.

[52] Aladejare, A. E., & Akeju, V. O. (2020). Design and Sensitivity Analysis of Rock Slope Using Monte Carlo Simulation. Geotechnical and Geological Engineering, 38(1), 573–585. doi:10.1007/s10706-019-01048-z.

[53] Chakraborty, R., & Dey, A. (2022). Probabilistic slope stability analysis: state-of-the-art review and future prospects. Innovative Infrastructure Solutions, 7(2), 177. doi:10.1007/s41062-022-00784-1.